# Characterizing the Natural History of Acute Radiation Syndrome of the Gastrointestinal Tract: Combining high mass and spatial resolution using MALDI-FTICR-MSI

**Claire L. Carter**[*], **Kim G. Hankey**[†], **Catherine Booth**[‡], **Gregory L. Tudor**[‡], **George A. Parker**[§], **Jace W. Jones**[*], **Ann M. Farese**[†], **Thomas J. MacVittie**[†], and **Maureen A. Kane**[*]

[*]University of Maryland, School of Pharmacy, Department of Pharmaceutical Sciences, Baltimore, MD USA

[†]University of Maryland, School of Medicine, Department of Radiation Oncology, Baltimore, MD USA

[‡]Epistem Ltd, Manchester, UK

[§]Charles River Laboratories, Pathology Associates, Raleigh-Durham, North Carolina, USA

## Abstract

The acute radiation syndrome of the gastrointestinal tract has been histologically characterized but the molecular and functional mechanisms that lead to these cellular alterations remain enigmatic. Mass spectrometry imaging is the only technique that enables the simultaneous detection and cellular or regional localization of hundreds of biomolecules in a single experiment. This current study utilized matrix-assisted laser desorption/ionization mass spectrometry imaging for the molecular characterization of the first natural history study of GI-ARS in the non-human primate. Jejunum samples were collected at days 4, 8, 11, 15 and 21 following 12 Gy partial body irradiation with 2.5% bone marrow sparing. Mass spectrometry imaging investigations identified alterations in lipid species that further understanding of the functional alterations that occur over time in the different cellular regions of the jejunum following exposure to high doses of irradiation. Alterations in phosphatidylinositol species informed on dysfunctional epithelial cell differentiation and maturation. Differences in glycosphingolipids of the villi epithelium that would influence the absorptive capacity and functional structure of the brush border membrane were detected. Dichotomous alterations in cardiolipins indicated altered structural and functional integrity of mitochondria. Phosphatidylglycerol species, known regulators of toll-like receptors, were detected and localized to regions in the lamina propria that contained distinct immune cell populations. These results provide molecular insight that can inform on injury mechanism in a non-human primate model of the acute radiation syndrome of the gastrointestinal tract. Findings may contribute to the identification of therapeutic targets and the development of new medical countermeasures.

**Correspondence:** Maureen A. Kane, Ph.D, Department of Pharmaceutical Sciences, University of Maryland School of Pharmacy, 20 N. Pine Street, Room N706, Baltimore, MD 21201, Phone: 410-706-5097, Fax: 410-706-5017, mkane@rx.umaryland.edu.

Conflicts of Interest:

Authors have no conflicts of interest to declare

**Keywords**

Biological indicators; imaging; radiation damage; gastrointestinal tract

## Introduction

Exposure to lethal doses of radiation results in dose- and time-dependent organ-specific sequelae (Booth et al. 2012b; Farese et al. 2012; MacVittie et al. 2012a; MacVittie et al. 2012b; Plett et al. 2012; Garofalo et al. 2014). In the acute time-scale (<60 days), doses below 10 Gy are lethal for the hematopoietic system and doses greater are lethal for the gastrointestinal system. Collectively, these are categorized as the acute radiation syndromes (ARS) of the gastrointestinal (GI-ARS) and hematopoietic (H-ARS) systems. Acute kidney injury has also recently been shown in doses above 10 Gy in our studies and in retrospective studies looking at clinical data from incidents involving accidental exposures to high-doses of radiation (Fliedner et al. 2005; Cohen et al. 2017). Whilst the dose required for lethality is lower for H-ARS, the duration of clinical symptoms and the time to mortality are longer than those observed for GI-ARS. Consequently, those who experience high-dose exposure will develop symptoms relating to gastrointestinal complications first. The time course of GI-ARS in the non-human primate is 1-15 days (d) post-exposure and is associated with nausea, vomiting, diarrhea, dehydration and weight loss (MacVittie et al. 2012a; MacVittie et al. 2012b). The denudation of the mucosal epithelial layer that occurs around day 6 enables bacterial translocation that can result in sepsis (Booth et al. 2012b; MacVittie et al. 2012b). Those that survive the first 15 d through medical intervention (rehydration and antibiotics) are already experiencing the coincident development of H-ARS(Farese et al. 2012; Plett et al. 2012). Medical management of H-ARS with blood transfusions, bone marrow transplantion or an FDA-approved medical countermeasure (MCM) such as Neupogen or Neulasta may increase survival leading to the development of the delayed effects of acute radiation exposure (DEARE) and multi-organ injury (MOI) involving the GI, kidney, heart and lungs (Booth et al. 2012a; MacVittie et al. 2012a; Farese et al. 2013; Farese et al. 2014; Garofalo et al. 2014; de Faria et al. 2015; Hankey et al. 2015; Medhora et al. 2015; Cohen et al. 2017). While each of these sequelae may result in high morbidity and mortality, understanding the biochemical mechanisms of GI-ARS for the development of medical countermeasures is of vital importance to enable survival within the first 2 weeks post-exposure. Additionally, understanding the development of the acute phase post-exposure may inform on the functional alterations that lead to the development of the prolonged GI damage and delayed multi-organ injury.

The GI-ARS has been extensively studied and there are known characteristics that center on loss of the stem cell niche leading to epithelial denudation(Potten et al. 1978; Potten and Booth 1997; Potten and Grant 1998; Roberts et al. 2003; Booth et al. 2004; Gandara et al. 2012). Surviving crypts then become hyper-proliferative to restore the epithelial mucosal barrier resulting in regenerated villi with altered functional capacity(Booth et al. 2012a; Booth et al. 2012b; MacVittie et al. 2012a; MacVittie et al. 2012b). The molecular mechanisms involved in these pathologies and what results in the development of chronic disease are not fully understood.

The MCART consortium has developed and characterized animal models that define the incidence, latency, severity and onset of GI-ARS, H-ARS, and MOI involving the kidney, lung, and heart (Farese et al. 2012; Jackson et al. 2012; Plett et al. 2012; Garofalo et al. 2014; de Faria et al. 2015; Farese et al. 2015; Medhora et al. 2015; Zhang et al. 2015; Cohen et al. 2017). Histological, clinical, and analytical techniques were used to interrogate mechanisms of action (MoA) and identify biomarkers of radiation injury following all-cause mortality (Booth et al. 2012a; Chua et al. 2012; MacVittie et al. 2012a; Jones et al. 2014a; Jones et al. 2014b; Carter et al. 2015; Farese et al. 2015; Jones et al. 2015; Zhang et al. 2015; Carter et al. 2016; Carter et al. 2017; Cohen et al. 2017; Jones et al. 2017). While these studies have provided vital mechanistic 'pieces of the puzzle' and identified panels of biomarkers that can be used to assess injury and efficacy of a MCM, they cannot inform on the natural history of injury development. The data is naturally skewed towards the most severe pathologies due to the humane euthanasia of animals based on the Institutional Animal Care and Use (IACUC)-approved criteria. Consequently, there are vital data missing that would enable elucidation of the mechanisms that lead to the development of certain pathologies.

The current study was designed to utilize matrix-assisted laser desorption/ionization mass spectrometry imaging (MALDI-MSI) to characterize the natural history of GI-ARS over a period of 21 d after high-dose irradiation. MALDI-MSI is an emerging molecular imaging technique that identifies histological regions and cellular content based on label-free detection of their biomolecular profiles. The ability to spatially localize lipids, metabolites, proteins, glycans, drugs and their active metabolites, in serial sections from resected organs and biopsies is putting MSI at the forefront of preclinical, clinical and drug development research(Carter et al. 2011; Palmer et al. 2012; Steven and Bunch 2013; Powers et al. 2015; Harvey et al. 2016; Carter et al. 2017; Drake et al. 2017; Hulme et al. 2017; Le Rhun et al. 2017; Lukowski et al. 2017; Nilsson et al. 2017). The application of high-resolution MSI to sections of the jejunum taken from control animals and at days 4, 8, 11, 15 and 21 post-exposure enabled the characterization of structural and functional lipids involved in physiological and pathological processes. Specific phospholipids were spatially localized to proliferating crypts and immune cell sub-populations, glycosphingolipids to the villi epithelium, and cardiolipins to inform on mitochondrial stability and function. Spatially localizing these lipids in control sections and mapping their alterations in the epithelium prior to denudation, and in the crypts and villi epithelium during regeneration, has enabled the identification of molecular species linked to functional mechanisms involved in injury severity and recovery. Information of this kind has not been ascertained previously.

## Material and Methods

### Materials

Analytical grade solvents, methanol (MeOH), chloroform ($CHCl_3$), isopropanol (IPA), tetrahydrofuran (THF), acetonitrile (ACN) and water ($H_2O$) were purchased from Fisher Scientific (Pittsburgh, PA, USA). Gelatin and 9-AA were purchased from Sigma-Aldrich (St. Louis, MO, USA). Hematoxylin and eosin (H&E) staining kit and the glass slides were purchased from Thermo Scientific (San Jose, CA, USA).

## Animals

Details of animal acclimation, housing and care were described in detail previously(MacVittie et al. 2012b). For MSI investigations, male rhesus macaques (*Macaca mulatta*, Chinese origin) received 12 Gy with 2.5% bone marrow sparing (PBI/BM2.5). For immunohistochemistry (IHC) studies, male rhesus macaques received 12 Gy with 5% bone marrow sparing (PBI/BM5). For all experiments the dose was delivered at 80 cGy min$^{-1}$ using a 6 megavolt (MV) photon beam from a clinical linear accelerator (LINAC). NHP were observed for clinical indices of GI damage including hydration status and fluid requirement, edema, oral mucositis, hematochezia, and frequency and severity of diarrhea. Pre-planned or timed euthanasia was at study day (SD) 4, 8, 11, 15 and 21 with n = 4 for each group. Tissue from two non-irradiated animals were used for the baseline control comparisons. All animal procedures were performed with prior approval from the University of Maryland's Institutional Animal Care and Use Committee (IACUC) and in accordance with the requirements as set forth in the United States Department of Agriculture (USDA) Animal Welfare Act (21 CFR Part 9), and the NIH Public Health Service Policy and Guide for the Care and Use of Laboratory animals.

## Immunohistochemistry

Immunohistochemistry was performed on 5 μm thick formalin-fixed paraffin embedded sections using the Discovery XT and Discovery Ultra research instruments (Ventana Medical Systems, Inc. Tucson, Arizona, USA). Sections were deparaffinized with Discovery EZ prep and then either heat retrieved with the proprietary solutions, Discovery RiboCC and Discovery CC1, or pretreated with Protease 2 (Ventana Medical Systems, Inc. Tucson, Arizona, USA) at 37°C. Sections were then incubated with either CD13 or Ki-67 primary antibodies (abcam, Cambridge, Massachusetts, USA). The concentrations, temperature and incubation times were based on protocols optimized with positive control tissues. A systematic protocol for each antibody is listed in supplementary Tables 1 and 2.

## Tissue Collection for MSI – The Swiss Roll Technique

Tissue was collected from the same region of the jejunum for all experiments. Fresh frozen blocks of jejunum were prepared using the Swiss roll technique as follows. Three to four inch sections of the jejunum were removed from the abdomen and immediately transferred into cold carbogenated Kreb's buffer. The sections were opened longitudinally and the contents carefully removed by gentle rinse in Kreb's buffer. Using a wooden applicator stick, each segment was rolled up longitudinally with the mucosa facing out, snap frozen in liquid nitrogen and stored at −80 °C.

## Tissue Preparation for Mass Spectrometry

To protect the mucosa and tissue integrity during sections the jejunum samples were embedded in gelatin as previously described(Carter et al. 2016). Jejunum samples were sectioned at 10 μm using a Thermo Microm HM 550 cryostat (Thermo Scientific, San Jose, CA, USA), with the chamber set to −20 °C, and transferred to positively charged histology slides. 9-AA at 10 mg mL$^{-1}$ in IPA:THF:H2O (4.5:4.5:1, v/v/v) was deposited over the

slides using the automated HTX sprayer (HTX Technologies, North Carolina, USA) as previously described(Carter et al. 2015).

Lipid washes for ultra performance liquid chromatography - high definition data independent tandem mass spectrometry (UPLC-HDMS$^E$) experiments, were prepared by pipetting 1 mL of chloroform/methanol (2:1 v/v) over two sections on a single glass slide, and collecting the run off. These experiments were for orthogonal fragmentation studies to enable structural elucidation of phospholipids.

### Lipid Structure Confirmation

Lipid extracts from the tissue washes were re-suspended in chloroform/methanol (1:1, v/v) and further diluted with isopropanol/acetonitrile/water (2:1:1, v/v/v) for analysis. Full details of the solvents and methods used for chromatographic separation and HDMS$^E$ fragmentation experiments were described in detail previously(Jones et al. 2017). Briefly, UPLC/HDMS$^E$ was performed on an ACQUITY UPLC system using a C18 CSH (1.7 μm; 2.1 × 100 mm) column (Waters, Milford, MA), coupled to a Waters SYNAPT G2-S traveling wave ion mobility enabled hybrid quadrupole time-of-flight mass spectrometer (Waters, Milford, MA). The instrument was operated in positive and negative ion modes over a mass range of, $m/z$ 200-1200.

### Mass Spectrometry Imaging

Imaging experiments were performed using a Bruker fourier transform ion cyclotron resonance (FTICR) mass spectrometer (Bruker Daltonics, Bremen, Germany) equipped with a dual ESI/MALDI ion source and Smartbeam II Nd:YAG (355 nm) laser. The instrument was operated within the mass range of $m/z$ 100-2000 in the negative ion mode, with a transient length of 0.5592 s, resulting in an estimated resolving power of 130,000 at $m/z$ 400 (FWHM). The instrument was calibrated using known matrix and lipid ions detected from an adjacent tissue section. On-line calibration during acquisition used the ion at $m/z$ 885.54983, a known phosphatidylinositol (PI) that is commonly detected as the base peak in negative ion mode tissue imaging studies, by MALDI-MS. Images were acquired summing 200 laser shots per position using the small laser setting and a 30 μm pixel size using the oversampling method(Jurchen et al. 2005). Following analysis sections were washed with solvents to remove the matrix and stained with hematoxylin and eosin (H&E). Slides were then scanned using the Aperio slide scanner (Leica Microsystems Inc., IL, USA) and images were correlated with the MALDI-MS data.

### Data Analysis

Data analysis was carried out using the SCiLS lab software suite version 2016b (SCiLS, Bremen, Germany) and FlexImaging version 4.0 (Bruker Daltonics, Billerica, MA, USA). Spectral analysis was carried out using Data Analysis software version 4.4 (Bruker Daltonics, Billerica, MA, USA). Data files were combined and imported as a single file into the SCiLS Lab software for comparison and statistical analysis. Component analysis was carried out on individual datasets using probabilistic latent semantic analysis (pLSA) with deterministic initialization to identify tissue structures based on molecular profiles. MS images were normalized using the root mean squared (RMS) algorithm and populated based

on ions from the component loadings. Identification of lipid species was based on a combination of fragmentation data from the HDMS$^E$ experiments and database searches using LipidMaps, The Human Metabolome Database (HMBD) and SwissLipids. Tentative lipid assignment was based on mass accuracies <3 ppm after external calibration using matrix and lipid ions.

## Results

### Histological Observations

An image of an H&E stained jejunum section in the Swiss roll orientation from one of the control animals is shown in Fig. 1A and a higher magnification image of a histologically labeled region is presented in Fig. 1B. Intestinal epithelial stem cells reside in the crypts of the small intestine where they divide to replenish villus epithelial cells (Potten and Grant 1998). They differentiate, mature and migrate along the crypt-villus axis (CVA), becoming terminally differentiated and senescent at or near the villus tip (Roberts et al. 2003; MacVittie et al. 2012a; MacVittie et al. 2012b). These cells are eventually shed into the gut lumen. The stem cell progenitors in the crypts differentiate into four epithelial populations: absorptive enterocytes, mucus-secreting goblet cells, enteroendocrine cells that secrete hormones and Paneth cells that secrete antimicrobial peptides (Peterson and Artis 2014). Paneth cells migrate distally to the bottom of the crypts whereas the remaining epithelial types migrate up the villus to the tip. Absorptive cells are the predominant cells of the villi epithelium; they are responsible for dietary fat and lipid absorption, which occurs at the brush border membrane of their apical surface(Wang et al. 2013). The lamina propria, located underneath the epithelium at the center of the villi and surrounding the crypts, is a region of loose connective tissue containing immune cell populations. This is the site of mucosal immunity. The muscularis mucosae is a thin layer of smooth muscle that separates the lamina propria from the submucosa. The submucosa is a layer of connective tissue that also contains ganglions and nerve fibers called the Meissner's plexus, which controls the contractions of the mucosa muscle layer. The muscularis externa is divided into the inner circular muscle layers and the outer longitudinal muscle layers, and this serves to propel ingesta through the intestine. Auerbach's plexus, the nerve tissue that runs in between the circular and longitudinal muscle layers, controls the muscle contraction responsible for propelling ingesta.

The H&E stained sections from the irradiated animals are shown in Figs. 1C and D. Fig. 1C is presented in the same order as the MSI images in the forthcoming sections and Fig. 1D displays high magnification regions of the crypt-villus axis (CVA) for injury comparison to the labeled control section presented in Fig. 1B. Histological characterization of acute GI injury in this model has been characterized previously(MacVittie et al. 2012a; MacVittie et al. 2012b) and will only be summarized here. At day 4 post-exposure there is a loss of crypts and villus blunting, the remaining crypts are small with few cellular elements. At day 8 there are very few crypts, severe villus blunting and an incomplete or denuded epithelial surface layer. The transition time of cells from the stem cell niche in the crypts to the villus tip under normal conditions was shown to be 7 d(MacVittie et al. 2012b), thus by day 8 post-exposure the loss of mucosal epithelium is due to interruption of cell production in the crypts. Crypt

loss was also shown to be most severe by day 6-7 in the TBI model(MacVittie et al. 2012b). By day 11 post-exposure crypts are evident but all are hyperplastic and the villi are starting to regenerate. At day 15 there are many crypts, most are hyperplastic and the villi are blunted with varying stages of regeneration evident. By day 21 two of the study animals presented with numerous, mostly hyperplastic crypts. One study animal at day 21, the animal designated 9724, presented with regenerating crypts that were hyperplastic and incomplete regeneration of the villi with a loss of epithelium in most places. Villus blunting occurred throughout the 21 d post-exposure and low cellularity in the lamina propria was noted in all animals from d8. The decrease in immune cell populations was likely caused by their marked radiosensitivity, thymic exposure and co-development of H-ARS at this dose and days post-exposure(Farese et al. 2012). One animal in the 21 day cohort did not survive and was euthanized for cause prior to the 21 d scheduled necropsy. The regions scanned during MSI acquisition are shown by the black lines in each stained section.

## Probabilistic Latent Semantic Analysis

Probabilistic latent semantic analysis (pLSA) with deterministic initialization was carried out on the individual datasets to identify tissue sub-compartments based on their mass spectral profiles. Five, seven and nine components were examined for each dataset. The seven components dataset was taken forward for comparison of the score images, as this number was optimal for histologically identifiable jejunum molecular profiles in the irradiated animals. Due to the number of study animals, representative score images for each day post-exposure were selected and are shown in Fig. 2, this enabled score images to be displayed in one figure. All pLSA score images for each animal post-exposure are presented in supplementary figure (SF) 1A-F. The score images from the control dataset showed the villi epithelium (components 1 & 4), the muscularis externa with reduced signal in the lamina propria (component 3), the crypts with lower intensity signal in the villi epithelium (component 5), and the laminal propria with most signal intensity at the villi tip (component 6). Components 2 and 7 are a mixture of matrix ions and tissue-related ions with little tissue specificity. At day 4 post-exposure there were score images correlating to the villi epithelium and muscularis externa (components 2 & 3, respectively). However, there was a significant shift in the identifiable tissue sub-compartments and these changes correlate well with the histological alterations. There was no score image relating to crypts in agreement with a lack of identifiable crypts by histology. There was strong signal highlighting the mucosal lamina propria but unlike those observed for the control samples, in the day 4 post-exposure sample this signal was intense throughout the lamina propria. (component 4). There was also a strong signal within the lamina propria of the crypt-region that appears to decrease in intensity in regions of dying crypts and showed lower signal intensity in the villi lamina propria (component 7). There was a loss of tissue-based structure in the day 8 score images compared to the control and day 4, and again this corresponded with histological observations. There was signal highlighting regions of blunted/denuded villi (components 1 & 7) and low signal in the lamina propria (component 6) but identifiable structure based on molecular profiles was lost. The muscularis externa was discernable by component 3. The remaining components were matrix-associated ions and tissue-related ions that show very little specific tissue distribution. Days 11, 15 and 21 post-exposure, with the exception of one animal at day 21, all displayed similar score images that again correlated well with

histological observations. There were score images distinct for crypt regions that were much larger and less structured than those presented in the control animals (components 4, 1 and 4, for days 11, 15 and 21, respectively). These score images corresponded to the hyperplastic crypts observed by histology. Days 11 and 15 still had reasonably intense signal in the lamina propria of the CVA (components 3 & 7 for day 11, and component 7 for day 15) and this was much less intense at day 21 post-exposure (component 7). Days 11 and 15 also displayed images corresponding to the submucosa (components 2).

The loadings for the components were used to populate the MS images in the forthcoming sections.

### Lipidomic Dysregulation

MALDI-MSI of control jejunum tissue revealed histologically distinct lipidomic distributions in the same manner as those observed for the lipidomic(Garate et al. 2015; Bestard-Escalas et al. 2016) and proteomic(Holzlechner et al. 2017) imaging studies of the colon. The spatial distributions identified by the component analysis were broadly defined as the CVA, the villi epithelium, the lamina propria, and the muscularis mucosa and externa. Manual interrogation of the datasets also identified lipid species distinct to Meissner's and Auerbach's plexus, regions of nerve tissue. Regional molecular specificity was impacted by lipid class and acyl chains, therefore each region will be discussed separately. In most instances, ether-linked phospholipids (PLs) and acyl-PLs with polyunsaturated fatty acids (PUFAs) were localized to the muscularis externa and the lamina propria, the latter of which is highly populated with immune cells. PLs with saturated, mono- and di-unsaturated fatty acids were localized to the CVA and several glycosphingolipids were highly localized to the villi epithelium. Structural elucidation of lipid fatty acyl chains based on the UPLC/HDMS$^E$ was possible for a number of species. A number of the ions detected by MALDI were not detected during the UPLC/HDMS$^E$ experiments due to low sensitivity of detection following sample dilution of lipid washes and different mass ranges used during data acquisition. These ions were tentatively assigned, where possible, based on accurate mass and database searches.

### The Crypt-Villus Axis

A number of phosphatidylethanolamine (PE) and phosphatidylinositol (PI) lipid species were highly localized to the epithelial cells of the CVA in the normal jejunum, with species predominantly showing a gradient that decreased in signal from the crypt to the villus tip. Representative images of several of these species along with their dysregulation following radiation insult is shown in Fig. 3 and SF 2. A full list of ions along with their tentative assignments and tissue distribution in control jejunal sections is shown in Table 1. These species mainly contained saturated, mono- or di-unsaturated fatty acids. For instance, PE(40:3), PI(34:1), PI(36:3), PI(36:2), PI(36:1), PI(38:6) and PI(38:2) were all detected with an intensity gradient that decreased from the crypt to the villi tip. Conversely, PE(16:0/18:2), PI(32:0), PI(36:4), and PI(40:6), showed the opposite trend with low to no signal in the crypts and increasing intensity along the CVA to the tip. Two PE's, PE(18:1/18:2) and PE(18:0/18:1) were detected with a near uniform distribution along the CVA, with PE(18:0/18:1) also detected in muscularis externa. These results correlate with previously

published MSI data reported for the lipidomic distribution in the colonic crypt regions(Bestard-Escalas et al. 2016). The studies by Bestard-Escalas et al(Bestard-Escalas et al. 2016) identified a signal gradient along the colonic crypt epithelium for PI's and PE's that contained saturated and di-unsaturated fatty acids. The lipidomic findings here also correlate with known jejunal mucosal physiology and previously published data reporting differential expression and abundance in genomic, proteomic and metabolomics profiles of the epithelial cells as they differentiate and mature along the CVA (Mariadason et al. 2005; Chang et al. 2008; Yang et al. 2016).

A significant difference was detected in all lipid species that were localized to the CVA following radiation insult. The majority of these lipids are still evident in the villi epithelium at day 4 post-exposure, but there was a loss in lipids highlighting crypt regions, correlating with the histological observations of crypt loss at this time-point. At day 8 there was a near complete loss in signal for these lipids, which correlates with the loss of cellular content and structure detected along the CVA in the stained sections and reported during model development(MacVittie et al. 2012b). Despite the presence of crypt cells and epithelial regeneration identified on day 11 post-exposure, there remained a substantial decrease in the intensity of PE(16:0/18:2) and PE(18:1/18:2), in the villi epithelium compared to the controls. These lipids highlighted some epithelial structure in two of the animals at day 21 but the signal was significantly lower compared to the control samples, as shown in Fig. 3 and SF 2. PE(40:3), which was highly localized to the crypt regions in the control sections, showed negligible signal at days 4 and 8 post-exposure, with variable very low signal recovery in two animals at day 11 and higher signal detected in one animal each at days 15 and 21 (SF 2). PI(32:0) demonstrated a significant reduction in the villi epithelium at day 4 post-exposure in three of the animals investigated and the signal for this lipid did not recover with the regenerating epithelium, as evidenced by the lack of signal for this ion in SF 2. The remaining PI's detected along the CVA in control animals showed varying levels of recovery at day 11 post-exposure, with signal localized to the hyperplastic crypt regions. At days 15 and 21 there was a marked increase in signal above those detected in control jejunum sections, as shown in Figs. 3 and SF 2. In addition to the significant increase in intensity, these lipids no longer showed a defined gradient running from the crypts to the villi, instead there is an increased and near uniform signal detected along the CVA for these animals with significant intensity in the hyperplastic crypt regions and at the villi tips. There was very little evidence of epithelial regeneration in the third animal at day 21 and this animal had a loss of epithelium, which also correlated to a loss of signal for all PE species detected.

The increase in PI's at days 15 and 21 was attributed to the larger hyperproliferative crypts as these regions and cell sizes were significantly increased compared to the control samples (Fig. 3). The alterations in the distribution of the PI's observed, with regard to the increased intensity at the villi tips, is believed to be due to the presence of immature epithelial cells or proliferative crypt cells populating the villi epithelium. Enterocytes mature while migrating up the villi to exert their absorptive functions. As hyperplastic crypts were attempting to regenerate the villi and there was severe villi blunting, it is thought that the cell populations were not maturing or were not fully matured before they reach the ends of the blunted villi. IHC staining for Ki67^{+} cells was carried out in a parallel 12 Gy PBI/BM5 study to evaluate the rate of proliferation in the crypt cells. The Ki67 stain for jejunal sections from control

and irradiated animals at days 6, 9 and 29 post-exposure are shown in Figs. 4A-D respectively. The control section showed Ki67$^+$ cells in the proliferating crypt regions only, at day 6 there was almost a complete loss of Ki67$^+$ cells, which correlated with the loss of crypts. At day 9 there was Ki67$^+$ staining in proliferative cells within crypts and extending along the superficial surface of the mucosa. The key correlative data was the presence of Ki67$^+$ cells extending up along the lateral edges of villi at day 29 post-exposure. This is in agreement with the lipidomic findings that suggested the villi epithelium is being populated with immature epithelial cells due to an increased rate of migration of proliferative crypt cells in the acute injury. These results also agree with those previously reported during the investigation into the development of the chronic GI syndrome(Shea-Donohue et al. 2016). In those studies a decrease in alkaline phosphatase (ALP), a marker of mature enterocytes, was detected in the jejunum.

### Villi Epithelium

A number of ions were detected that were highly localized to the villi epithelium, as shown in Figs. 5 and SF 3. A full list of ions detected with high specificity to the villi epithelium is shown in Table 2. Over half of the ions were tentatively identified as sulfatides based on accurate mass and their distribution. The villi epithelium, and the apical membrane of polarized epithelial cells throughout the whole GI tract, have an unusually high amount of glycosphingolipids (GSLs)(Breimer et al. 1982a; Jennemann et al. 2012). The remaining ions could not be identified and have not been assigned, but they are believed to be GSLs that are yet to be identified and/or GSLs that are forming unusual ion formations, as database searches of the [M-H]$^-$, [M-H$_2$O]$^-$, [M-CH$_3$]$^-$, [M-2H+Na]$^-$, and [M-2H+K]$^-$ did not return any lipids that could be sensibly assigned within 5 ppm. Additionally, several of these ions were also detected in the Auerbach's plexus and nervous tissue that is known to have high concentrations of GSLs. The ions at $m/z$ 812.51852, 840.54999, 868.5812, 888.56969, 896.61293, 910.62931, 920.61441, 922.62941 and 924.65155 were all detected with high abundance outlining the villi epithelium in control jejunum samples. The ions at $m/z$ 812 and 840 were detected with higher abundance at the base and mid-villi epithelium and lower abundance towards the tip. Further investigation for their tentative identification was not carried out.

Dysregulation of all ions localized to the villi epithelium was apparent following radiation insult. At day 8 post-exposure there was little signal for these ions, correlating with the loss of villi epithelium observed in the histological sections. At day 4 and days 11-21 a difference in response was observed for sulfatides that appeared to depend on the sphingoid base and double bond number. Interestingly, the sulfatides with the unsaturated sphingosine base increased following injury and this trend was observed at day 4 post-exposure, before the villi epithelium was lost and days 11-21 when the epithelium was being regenerated. The sulfatides that contained saturated carbon chains in their sphingoid bases predominantly presented a decrease in intensity at every study day post-exposure despite the presence of villi at days 11-21. There were instances when one or two animals at days 11 and 15 showed a similar intensity to those detected in the sections from controls, as shown in Fig. 4 for ST(d34:0) and SF 3. The unidentified ions, believed to be glycosphingolipids, were all reduced at every study day post-exposure compared to the control animals. There were

animals at days 11, 15 and 21 post–exposure that had minimal signal for all ions detected along the villi epithelium even though there was histologically identifiable villi epithelium. The histological evaluation of jejunal sections from these animals revealed worse disease pathology or less structured villi epithelium compared to other animals within their cohorts.

The uniquely abundant GSL content of the villi epithelium has been well-established and decades of research has provided information regarding their composition and functional importance across species(Breimer et al. 1982b; Dahiya et al. 1986; Breimer et al. 2012). The GSL dysregulation observed here will have a profound effect on the structure and function of the enterocyte brush border membrane(Delacour et al. 2005; Jennemann et al. 2012). To assess the impact of GSL dysregulation CD13 IHC labeling was used. CD13 is a zinc-binding metalloprotease that is located on epithelial cells of the kidney and intestines(Dixon et al. 1994). In the NHP, jejunum positive labelling for this marker was located on the brush border of the villi, thus providing a strong indication of the functional absorptive area. The CD13 IHC results are shown in Figs. 6A-D for control, and days 8, 11 and 19 post-irradiation, respectively. CD13^{+} positive staining can be observed in the villi epithelium and brush border from the base to the villi tip in the tissue taken from control animals. At day 8 post-exposure there was staining in the brush border in the severely blunted epithelium. By day 11 there were very few CD13^{+} cells in the regenerating villi epithelium and marginal staining that showed evidence of regenerating regions of a brush border. At day 19 post-exposure there was CD13^{+} staining in the brush border but this was not uniform compared to those seen in the control sections and there was no staining in the epithelium. These results correlated with the GSL and CVA lipidomic findings that suggested a phenotypic or a structural and functional difference in the cell population of the villi epithelium during the acute phase of disease development.

### Lamina Propria and Muscularis Externa

The lamina propria is home to the mucosal immune system and is highly populated with immune cells under physiological conditions. This region, along with the muscularis externa shared a similar and distinctive lipidomic profile that predominantly consisted of phosphatidylglycerols (PG's), ether-linked PE's, and PI's and PE's that contained PUFAs (Fig. 7 and Table 3). These lipids were either highly abundant in the lamina propria with significantly lower signal in the muscle layers or highly abundant in the muscularis with a significantly lower signal in the lamina propria. There were also instances where the signal was high in both the lamina propria and the muscularis externa. For the most part, the distribution within these areas appeared to correlate with head group structures. For example, PE(42:5)/PE(O-42:6(OH))/PE(P-42:5(OH), PE(P-18:0/20:4), PE(18:0/20:4), PE(40:4) and PE(40:5) were detected with highest intensity in the muscularis externa followed by much lower intensity signal in the lamina propria of control sections. PI(38:4) and PI(38:5) were detected with a relatively even distribution in the lamina propria and muscularis externa, with lower signal in the submucosa. PI(40:4) and PI(40:5) in the control sections were detected with a slightly lower signal in the muscularis externa compared to the lamina propria. Representative images of PE and PI species detected in the lamina propria and muscularis externa of control and irradiated animals is shown in SF 4. The PE lipid species in the control jejunum sections that were detected predominantly in the muscularis

and lamina propria demonstrated variable alterations at each day post-exposure that appeared to be animal dependent. PE(P-18:0/20:4) appeared to increase slightly in the lamina propria and muscularis layers at days 4 and 8 post-exposure, with a decrease in signal observed in a number of sections at days 11-21 post-exposure, but again this appeared to be animal dependent. PI species show a more defined increase in intensity along the crypt regions of the lamina propria at days 4 and 8 post-exposure but this increase in intensity may be artificial and due to the reduction in tissue complexity attributed to the lack of crypts and cellular content. The larger acyl chain PI's demonstrated more significant reductions from day 8 onwards, but these were again variable and animal dependent. This variability may be due to the level of epithelial loss and regeneration within each animal and the co-development of radiation-induced lymphocytopenia and H-ARS that had a dramatic impact on the immune cell population of the jejunum and whole GI(Booth et al. 2012b; Farese et al. 2012; MacVittie et al. 2012b; Wang et al. 2015).

The most interesting finding in the lamina propria and muscularis regions in the control and irradiated animals was the distribution of PG species that were highly specific and these appeared to be attributed to their fatty acid profiles (Fig. 7). In the control sections PG(16:0/18:1) displayed highest intensity in the lamina propria surrounding the crypts followed by low intensity in the villi laminal propria and muscularis externa. PG(34:0) was detected with highest intensity in the muscularis externa followed by much lower intensity in the lamina propria. PG(18:2/18:2) and PG(18:1/18:2), both containing di-unsaturated FAs displayed a highly localized distribution in the lamina propria at the villus tip, with much lower signal intensity in the rest of the lamina propria and little to no signal in the muscularis externa. These specific distributions within the lamina propria are believed to be associated with distinct populations of immune cells as the villi tip in NHP were shown to contain predominantly macrophages, a phenomenon only observed in macaques(Bronson 1981). Whereas the lamina propria surrounding the crypt regions were populated with lymphocytes and a few neutrophils and monocytes, and the increased detection of PG(16:0/18:1) here was believed to be associated with these cells. The distribution of the PG species detected in control tissue and their alterations at each day post-exposure is shown in Fig. 7. For all PG species detected there was a significant difference in intensity at every day and in every animal post-exposure. PG(16:0/18:1) was detected with lower intensity in the irradiated animals that started at day 4 and remained low for the other study days examined. This lipid was barely detectable in two of the animals, one at day 4 and one at day 8, and these again correlated with the most severe disease pathology at each day. PG(34:0) was significantly increased in every animal at day 8 and one animal at day 11 post-exposure as shown in Fig. 7. The increase was observed in the muscularis externa, the submucosa, the muscularis mucosa and the regions of lamina propria remaining after irradiation. The remaining animals at day 11 and days 15-21 in comparison to the control displayed reduced signal intensity in the lamina propria and reduced or similar intensity in the muscularis externa. Again the animal at day 21 with the most severe pathology displayed minimal signal for this lipid. PG(18:2/18:2) and PG(18:1/18:2) were significantly reduced from day 8 post-exposure with some recovery in signal intensity observed at day 21 but these were not structured despite the presence of a regenerated epithelium in two of the animals. One

animal at day 4 had increased levels of all PG's detected and this is believed to be attributed to the lipidomic and cellular profile of the individual animal.

### Mitochondria

Cardiolipin is a unique tetra-acylated diphosphatidylglycerol that is highly specific for mitochondrial membranes where it predominantly resides in the inner membrane and is vital for functional processes and structural stability of mitochondria(Kagan et al. 2009; Balasubramanian et al. 2015; Kagan et al. 2015). We detected a number of cardiolipin species that demonstrated distinct distributions within the jejunum as shown in Fig. 8, Table 4 and SF5. The most abundant species in the control samples centered on the more commonly reported ions at $m/z$ 1445-1454 and these demonstrated distinct distributions based on double bond numbers in their acyl chains. CL(72:9) at $m/z$ 1445.9499 was localized to the crypt regions with a decreasing gradient along the CVA and no signal detected at the villi tip. CL(72:8) at $m/z$ 1447.9693 was detected with high intensity in the CVA, muscularis mucosa, and very low signal in the submucosa and lamina propria. CL(72:8) was the most abundant species detected and the detection here agreed with the detection of CL(18:2)$_4$ at $m/z$ 1447.9, during an investigation into oxidized cardiolipins in the small intestine, following radiation insult in a mouse model(Samhan-Arias et al. 2012b). CL(72:7) at $m/z$ 1449.9804 was detected with high intensity long the CVA with lower intensity in the muscularis mucosa. CL(72:6) at $m/z$ 1451.9943 was highly localized to the CVA showing a decreasing gradient along the axis to the villi tip. CL(72:5) at $m/z$ 1454.0079 was also highly localized to the CVA but this species was detected with very low abundance in the crypt and villi base region only. Representative images of the CL species detected and their alterations following radiation injury are presented in Fig. 8 and SF5. Following radiation injury CL(72:9), CL(72:8) and CL(72:7) decreased in all animals at each day post-exposure, with the exception of one animal at day 4. Interestingly, this was the same animal that showed increased intensity of all PG species and as CLs are derived from PGs(Chicco and Sparagna 2007) this is again believed to be animal specific due to higher amounts of these lipids within the jejunum of this animal. Conversely, CL(72:6) and CL(72:5) were decreased in the animals at day 4 and 8 post-exposure in agreement with the loss of crypts and epithelial cells of the CVA, but showed an increase in intensity in the CVA of several of the animals at days 11-21. These results correlate with those observed for the PI species that shared the same tissue distribution and were more highly distributed in the crypt regions of control animals. The animals that had little to no signal for the PLs in the CVA and the GSLs in the villi epithelium also had little to no signal for all CL species detected. The animals at day 8 and 21 that displayed little signal had reduced crypts and a denuded epithelium and thus the lack of signal is associated with a lack of cellular content. Conversely, the animals at days 11 and 15 did have hyperplastic crypts and regenerating epithelium. Therefore, the significantly reduced signal in these animals is consistent with dysregulated structural and functional mitochondria within these cells.

A significant shift in cardiolipin profiles was detected in the irradiated animals compared to the controls. An increase in shorter acyl-chain CLs was detected in the irradiated samples from day 8 onwards, with the exception of the animals that showed decreased intensity of most lipids detected. CL(70:7), CL(70:6), CL(70:5), and CL(70:4), were detected with

relatively high intensity in the CVA of the irradiated animals compared to the low intensity detected in the control animals. The shift to increased shorter chain CLs at days 8-21, when the crypts and villi are regenerating is indicative of alterations in mitochondrial function within these cells.

### Auerbach's and Meissner's Plexus - Neuronal Tissue

Several of the sulfatides detected in the epithelium were also detected in the jejunal neuronal tissue, which is unsurprising, as neuronal tissue is known to contain high concentrations of GSLs. Several GSLs were detected that were highly specific for jejunal nerve tissue and examples of these are shown in SF 6 and Table 5. The natural distribution of the neuronal cell populations in the jejunum makes it difficult to ascertain if there were any alterations in neuronal GSLs following radiation insult. As the cells appeared sporadically in histological sections it is too difficult to determine if differences in GSL signals were consequent to radiation injury or merely reflective of differential abundances of neuronal cells due to tissue sampling between the samples.

## Discussion

The application of MALDI-MSI to aid in characterization of the GI-ARS has identified a number of significant lipidomic alterations that will have a profound impact on intestinal function. Specifically, the alterations detected in the lipidomic species of the crypt and villus epithelium inform on dysregulated function and injury mechanism. Alterations in the CVA at days 4 and 8 will only be discussed in terms of changes that related to the cell populations present. At day 4, this was the villi epithelium as the crypts have lost cellular content. At day 8 post-exposure it was difficult to relate alterations in lipidomic profiles to cellular regions as there was a significant loss of proliferating crypt cells and villi epithelium. However, several results were indicative of enhanced proliferation in two of the animals at day 8.

The increased intensity of PI's at days 11-21 combined with Ki67^{+} proliferative cells along the villi epithelium and at the tip was indicative of undifferentiated or immature cells populating the epithelium. While this may confer some barrier protection to reduce translocation of bacterial and food toxins, these cells will have vastly different functional capabilities compared to normal absorptive enterocytes. This was further evidenced by the detection of alterations in GSLs within the villi epithelium following radiation insult and the loss of a functional brush border that was demonstrated using CD13 staining. The uniquely high composition of GSLs in the villi epithelium is essential to the absorptive and functional capacity of these cells(Jennemann et al. 2012). Jennemann et al (Jennemann et al. 2012) developed an enterocyte-specific GSL knockout (KO) mouse model that demonstrated GSLs were vital for absorption and intracellular transport of dietary fats and lipids. Newborn mice from the GSL KO model did not gain weight and died by post-natal day 8 and mice in the adult KO model showed a drastic decrease in body weight. Both newborn and adult GSL KO models demonstrated blunted villi that lacked a functional brush border and both had Ki67^{+} cells in their villi epithelium that were not observed in controls, similar to the observations reported in this GI-ARS model. The authors of the GSL KO study hypothesized that altered lipid absorption may lead to prolonged crypt cell hyperplasia and enhanced proliferation that

then inhibits epithelial differentiation and maturation. The results presented herein for the NHP model of GI-ARS draw a parallel with the GSL KO mouse study in many ways. The alterations in GSLs, which begin at day 4 post-exposure in the NHP and continues after crypt and villi regeneration, may be responsible for the crypt cell hyperplasia and immature blunted villi observed during the acute phase of GI-ARS. Results also demonstrated that radiation significantly altered GSL profiles in enterocytes as these alterations were evident at day 4 post-exposure, before the loss of villi due to the loss of proliferating crypts. The decrease in GSLs observed at day 4 may lead to a reduction of dietary fat and lipid absorption as these lipids have been shown to be essential for this function(Sillence and Platt 2004; Jennemann et al. 2012). A loss in GSL-dependent lipid absorption may be a causative factor for the early and continued weight loss reported(Booth et al. 2012a; Booth et al. 2012b; MacVittie et al. 2012a; MacVittie et al. 2012b; Cui et al. 2016; Shea-Donohue et al. 2016). GSLs are also vital for lipid raft formation, which is enriched in the microdomains of the apical brush border of enterocytes(Danielsen and Hansen 2013). Alterations in GSLs observed here would potentially impact raft formation and protein stability in the rafts, and also have deleterious effects on the protective properties of the membrane that are essential to prevent damage from luminal gut contents such as bile salts(Michael Danielsen and Hansen 2006; Danielsen and Hansen 2013). The GSL results observed herein may also inform on radiation-induced damage of functional epithelial cells in other organs that contain a brush border and abundant GSLs, such as the kidney(Cohen et al. 2017).

Another significant finding that will impact the functional capabilities of the jejunum, is the alterations in cardiolipin species in both the epithelium and the smooth muscle regions following radiation injury. CLs were shown to interact with and/or stabilize a number of proteins in mitochondria including key components of the electron transfer chain, substrate carriers and membrane proteins(Santucci et al. 2014; Li et al. 2015; Planas-Iglesias et al. 2015; Duncan et al. 2016; Vergeade et al. 2016). Through these interactions CLs play essential roles in membrane structure and organization, the respiratory chain and energy metabolism, mitophagy, and apoptosis(Paradies et al. 2014). Alterations in CL concentration or their fatty acid composition are associated with changes in mitochondrial structure and function, and have been linked to numerous pathological process that include Barth syndrome, pulmonary hypertension, heart failure and diabetes(Schlame and Ren 2006; Chicco and Sparagna 2007; Claypool and Koehler 2012; Raja and Greenberg 2014). Dysfunctional mitochondria due to CL oxidation and fatty acid remodeling is associated with the damage and severity of myocardial infarctions(Petrosillo et al. 2009). Reduction in CL oxidation using antioxidants such as melatonin during ischemia and reperfusion of the myocardium protected the muscle from injury(Petrosillo et al. 2009). Oxidation of CLs has also been shown to be involved in radiation-induced lung and small intestine injury in mouse models(Tyurina et al. 2011; Samhan-Arias et al. 2012a). The reduction of CLs in the muscularis externa reported here may have a detrimental impact on the function and respiration capacity of mitochondria in the muscle cells, thereby impacting GI motility. Mitochondrial dysfunction may also be responsible for crypt cell death and thus treatment aimed at protecting mitochondrial function through reduction of cardiolipin oxidation and fatty acid remodeling may confer protection to radiation-induced crypt sterilization and mitigate intestinal injury.

Not all of the CL fatty acid alterations detected are believed to be detrimental to mitochondrial function and stability, and thus cellular integrity. Changes observed in the CVA from day 8 post-exposure may be beneficial and pertinent to survival. The detection of a shift in the carbon number of the fatty acyl chains of CLs post-exposure and their increased localization to the proliferating cells of the CVA, correlates with the recent findings in highly proliferative activated immune cells, and aberrantly proliferating cancer cells(Schild et al. 2012; Sapandowski et al. 2015; Zhang et al. 2016). A study on the proliferation of lymphocytes, and prostate and thyroid cancer cells, all found a reduction in $CL(18:2)_4$ and an increase in C16 fatty acids in CLs detected from these cells compared to non-proliferating and non-cancer cells. The authors of these studies suggested a functional link between CL acyl-chain composition and cell proliferation. The changes in cardiolipin composition detected in this GI-ARS study correlate with these studies and may actually be an indicator of increased survival in the animals that demonstrated this functional shift to enable increased proliferation for restoration of the epithelium and barrier function. This finding was especially important in the animals that shared similar histology but had clear differences in lipid profiles and thus functional capacity. Damage to mitochondria that resulted in a reduction or loss of CLs, in the manner observed for several animals from day 4 post-exposure, may be a contributing factor to injury mechanism of GI-ARS. Several of these animals demonstrated proliferating crypts and varying levels of epithelial regeneration yet their lipid species remained significantly reduced compared to controls and other animals in their cohort. Therapeutics aimed at maintaining cardiolipin and mitochondrial integrity may protect these animals from radiation injury and enable a more rapid functional recovery of the epithelium. Cardiolipin fatty acids may also be important for differentiation and maturation of enterocytes as mitochondrial bioenergetics and CL remodeling enzymes were previously shown to play key roles in cell differentiation(Wang et al. 2007; Kasahara and Scorrano 2014). Medical intervention aimed at altering enterocyte CL fatty acid composition, thereby altering mitochondrial bioenergetics, may restore normal barrier functional activities by triggering differentiation.

It is difficult to interpret the reduction in lipids that relate to the immune cells of the lamina propria following radiation insult because of the coincident radiation effects on the thymus, radiosensitive circulating lymphocytes and the development of the H-ARS that reduced the levels of all circulating and tissue-based immune cell populations. For this reason, the reduction of ether-linked PLs and PLs with PUFAs in the lamina propria will not be discussed.

The detection of PG species highly localized to the tip of the lamina propria in control tissue may be useful markers of macrophages with distinct phenotypes. The intestinal mucosa has the largest reservoir of macrophages and the villi tip of the rhesus macaque has been shown to contain a high number of macrophages. The images of PG(18:2/18:2) and PG(18:1/18:2) presented here correlate with the images of macrophages in the villi tips as reported by Bronson et al (Bronson 1981). PG(16:0/18:1) distributed in the lamina propria around the crypts and PG(18:2/18:2) and PG(18:1/18:2), distributed in the lamina propria at the villi tips, demonstrated some recovery in several animals at days 15 and 21. Again this is difficult to interpret in terms of GI injury due to the development of H-ARSand radiation sensitivity of lymphocytes but it would appear there was at least some recovery in these animals.

PG species are also known to play keys roles in the suppression of inflammation through selective binding to toll-like receptors (TLRs) and components of their signaling pathways (Kuronuma et al. 2009; Kandasamy et al. 2011). Studies identified PG(16:0/18:1), as the predominant species in lung surfactant responsible for inhibiting lung inflammation following LPS stimulation (Kuronuma et al. 2009) and infection with *Mycoplasma pneumoniae* (Kandasamy et al. 2011) and the respiratory syncytial virus (Numata et al. 2010), in mouse models. Kuronuma et al (Kuronuma et al. 2009) identified CD14 and MD-2 as the high-affinity binding targets of PG(16:0/18:1) in alveolar macrophages, which prevented their interaction with TLR4, and inhibited downstream signaling to suppress inflammation. A recent in vitro study also demonstrated the anti-inflammatory actions of PG(18:1/18:1) and PG(18:2/18:2) in macrophage-like RAW264.7 cells (Chen et al. 2018). Collectively, these studies highlight the important functions that PGs play in regulating the innate immune system. The PGs detected and localized to specific regions of the lamina propria in this current study are believed to play central roles in the regulation of TLRs under physiological conditions by acting as TLR inhibitory molecules in a similar manner to those observed in the lung. TLRs in gut health and homeostasis have become the focus of much attention due to the close proximity of the intestinal immune populations with luminal food toxins and pathogen-associated molecular patterns (PAMPs) (Abreu et al. 2005). There is a stringent requirement to ensure there isn't aberrant immune activation and dysregulated inflammation caused by exposure to PAMPs. Additionally, prophylactic administration and post-exposure administration of compounds that manipulate TLR signaling and functions were shown to mitigate radiation injury in the intestine (Ciorba et al. 2012; Takemura et al. 2014). The functional roles of the species specific PGs detected within the different regions of the lamina propria and their interactions with TLRs need to be elucidated.

Dietary lipids were previously shown to impact the lipid composition of the plasma membrane of cells(Clamp et al. 1997). The authors do not believe that to be the case here due to the alterations in GSLs that would impact lipid absorption into the enterocytes. This was demonstrated in the GSL KO study as increased GSL in the diet of mice was not absorbed and did not alter the lipidomic profiles or restore the functional capacity of the enterocytes(Jennemann et al. 2012). Alterations in lipid absorption due to GSL reduction, in combination with the previously reported reduction in glucose absorption, are thought to be responsible for the weight loss observed after high-doses of irradiation(Booth et al. 2012a; Booth et al. 2012b; MacVittie et al. 2012a; MacVittie et al. 2012b). Additionally, the dysfunctional uptake of dietary nutrients by enterocytes suggests that the medical management of liquid meal supplements used when animals lost a significant amount of body weight, may not have been absorbed efficiently. These findings may be contributing factors to euthanasia of animals due to severe BW loss and radiation-induced cachexia(Cui et al. 2016).

## Conclusion

In summary, we have identified structural, functional and mechanistic lipidomic alterations in the jejunum following radiation insult that may open new avenues for the investigation of medical countermeasures and medical management. Future studies should focus on the pleiotropic activities of cardiolipin, particularly at days 1-4 post-exposure, and during the

regeneration of the mucosa. Antioxidants, such as melatonin, that have conferred protection from cell death through stabilization of mitochondrial cardiolipin may show protection in this radiation injury model. Therapeutic interventions aimed at altering CL fatty acid composition and mitochondrial bioenergetics, such as those shown using acetaminophen (Vergeade et al. 2016), may restore the functional capacity of enterocytes by triggering epithelial differentiation and maturation. Lastly, the role of PG's in the regulation of mucosal immunity and radiation-induced injury needs further investigation as these lipids may prove to be effective medical countermeasures.

## Supplementary Material

Refer to Web version on PubMed Central for supplementary material.

## Acknowledgements

## References

Abreu MT, Fukata M, Arditi M. TLR signaling in the gut in health and disease. Journal of immunology (Baltimore, Md : 1950) 174: 4453–60; 2005.

Balasubramanian K, Maeda A, Lee JS, Mohammadyani D, Dar HH, Jiang JF, St Croix CM, Watkins S, Tyurin VA, Tyurina YY, Kloditz K, Polimova A, Kapralova VI, Xiong Z, Ray P, Klein-Seetharaman J, Mallampalli RK, Bayir H, Fadeel B, Kagan VE. Dichotomous roles for externalized cardiolipin in extracellular signaling: Promotion of phagocytosis and attenuation of innate immunity. Science signaling 8: ra95; 2015. [PubMed: 26396268]

Bestard-Escalas J, Garate J, Maimo-Barcelo A, Fernandez R, Lopez DH, Lage S, Reigada R, Khorrami S, Ginard D, Reyes J, Amengual I, Fernandez JA, Barcelo-Coblijn G. Lipid fingerprint image accurately conveys human colon cell pathophysiologic state: A solid candidate as biomarker. Biochimica et biophysica acta 1861: 1942–1950; 2016. [PubMed: 27663183]

Booth C, Booth D, Williamson S, Demchyshyn LL, Potten CS. Teduglutide ([Gly2]GLP-2) protects small intestinal stem cells from radiation damage. Cell proliferation 37: 385–400; 2004. [PubMed: 15548172]

Booth C, Tudor G, Tonge N, Shea-Donohue T, MacVittie TJ. Evidence of delayed gastrointestinal syndrome in high-dose irradiated mice. Health Phys 103: 400–10; 2012a. [PubMed: 23091877]

Booth C, Tudor G, Tudor J, Katz BP, MacVittie TJ. Acute gastrointestinal syndrome in high-dose irradiated mice. Health Phys 103: 383–99; 2012b. [PubMed: 23091876]

Breimer ME, Hansson GC, Karlsson KA, Larson G, Leffler H. Glycosphingolipid composition of epithelial cells isolated along the villus axis of small intestine of a single human individual. Glycobiology 22: 1721–30; 2012. [PubMed: 22833314]

Breimer ME, Hansson GC, Karlsson KA, Leffler H. Glycosphingolipids of rat tissues. Different composition of epithelial and nonepithelial cells of small intestine. The Journal of biological chemistry 257: 557–68; 1982a. [PubMed: 7053385]

Breimer ME, Hansson GC, Karlsson KA, Leffler H. Studies on differentiating epithelial cells of rat small intestine. Alterations in the lipophilic part of glycosphingolipids during cell migration from crypt villus tip. Biochimica et biophysica acta 710: 415–27; 1982b. [PubMed: 7074122]

Bronson RT. Ultrastructure of macrophages and karyolytic bodies in small intestinal villi of macaque monkeys and baboons. Veterinary pathology 18: 727–37; 1981. [PubMed: 6270871]

Carter CL, Jones JW, Barrow K, Kieta K, Taylor-Howell C, Kearney S, Smith CP, Gibbs A, Farese AM, MacVittie TJ, Kane MA. A MALDI-MSI Approach to the Characterization of Radiation-Induced Lung Injury and Medical Countermeasure Development. Health Phys 109: 466–78; 2015. [PubMed: 26425906]

Carter CL, Jones JW, Farese AM, MacVittie TJ, Kane MA. Inflation-Fixation Method for Lipidomic Mapping of Lung Biopsies by Matrix Assisted Laser Desorption/Ionization-Mass Spectrometry Imaging. Analytical chemistry 88: 4788–94; 2016. [PubMed: 27028398]

Carter CL, Jones JW, Farese AM, MacVittie TJ, Kane MA. Lipidomic dysregulation within the lung parenchyma following whole-thorax lung irradiation: Markers of injury, inflammation and fibrosis detected by MALDI-MSI. Sci Rep 7: 10343; 2017. [PubMed: 28871103]

Carter CL, McLeod CW, Bunch J. Imaging of Phospholipids in Formalin Fixed Rat Brain Sections by Matrix Assisted Laser Desorption/Ionization Mass Spectrometry. Journal of the American Society for Mass Spectrometry 22: 1991–1998; 2011. [PubMed: 21952770]

Chang J, Chance MR, Nicholas C, Ahmed N, Guilmeau S, Flandez M, Wang D, Byun DS, Nasser S, Albanese JM, Corner GA, Heerdt BG, Wilson AJ, Augenlicht LH, Mariadason JM. Proteomic changes during intestinal cell maturation in vivo. Journal of proteomics 71: 530–46; 2008. [PubMed: 18824147]

Chen W-W, Chao Y-J, Chang W-H, Chan J-F, Hsu Y-HH. Phosphatidylglycerol Incorporates into Cardiolipin to Improve Mitochondrial Activity and Inhibits Inflammation. Scientific Reports 8: 4919; 2018. [PubMed: 29559686]

Chicco AJ, Sparagna GC. Role of cardiolipin alterations in mitochondrial dysfunction and disease. American journal of physiology Cell physiology 292: C33–44; 2007. [PubMed: 16899548]

Chua HL, Plett PA, Sampson CH, Joshi M, Tabbey R, Katz BP, MacVittie TJ, Orschell CM. Long-term hematopoietic stem cell damage in a murine model of the hematopoietic syndrome of the acute radiation syndrome. Health Phys 103: 356–66; 2012. [PubMed: 22929468]

Ciorba MA, Riehl TE, Rao MS, Moon C, Ee X, Nava GM, Walker MR, Marinshaw JM, Stappenbeck TS, Stenson WF. Lactobacillus probiotic protects intestinal epithelium from radiation injury in a TLR-2/cyclo-oxygenase-2-dependent manner. Gut 61: 829–838; 2012. [PubMed: 22027478]

Clamp AG, Ladha S, Clark DC, Grimble RF, Lund EK. The influence of dietary lipids on the composition and membrane fluidity of rat hepatocyte plasma membrane. Lipids 32: 179–84; 1997. [PubMed: 9075208]

Claypool SM, Koehler CM. The complexity of cardiolipin in health and disease. Trends in biochemical sciences 37: 32–41; 2012. [PubMed: 22014644]

Cohen EP, Hankey KG, Bennett AW, Farese AM, Parker GA, MacVittie TJ. Acute and Chronic Kidney Injury in a Non-Human Primate Model of Partial-Body Irradiation with Bone Marrow Sparing. Radiation research 188: 661–671; 2017. [PubMed: 29035153]

Cui W, Bennett AW, Zhang P, Barrow KR, Kearney SR, Hankey KG, Taylor-Howell C, Gibbs AM, Smith CP, MacVittie TJ. A non-human primate model of radiation-induced cachexia. Sci Rep 6: 23612; 2016. [PubMed: 27029502]

Dahiya R, Brown MD, Brasitus TA. Distribution of glycosphingolipids of monkey small and large intestinal mucosa. Lipids 21: 107–111; 1986. [PubMed: 3959770]

Danielsen EM, Hansen GH. Generation of Stable Lipid Raft Microdomains in the Enterocyte Brush Border by Selective Endocytic Removal of Non-Raft Membrane. PLOS ONE 8: e76661; 2013. [PubMed: 24124585]

de Faria EB, Barrow KR, Ruehle BT, Parker JT, Swartz E, Taylor-Howell C, Kieta KM, Lees CJ, Sleeper MM, Dobbin T, Baron AD, Mohindra P, MacVittie TJ. The Evolving Mcart Multimodal

Imaging Core: Establishing a Protocol for Computed Tomography and Echocardiography in the Rhesus Macaque to Perform Longitudinal Analysis of Radiation-Induced Organ Injury. Health Phys 109: 479–92; 2015. [PubMed: 26425907]

Delacour D, Gouyer V, Zanetta JP, Drobecq H, Leteurtre E, Grard G, Moreau-Hannedouche O, Maes E, Pons A, Andre S, Le Bivic A, Gabius HJ, Manninen A, Simons K, Huet G. Galectin-4 and sulfatides in apical membrane trafficking in enterocyte-like cells. The Journal of cell biology 169: 491–501; 2005. [PubMed: 15883199]

Dixon J, Kaklamanis L, Turley H, Hickson ID, Leek RD, Harris AL, Gatter KC. Expression of aminopeptidase-n (CD 13) in normal tissues and malignant neoplasms of epithelial and lymphoid origin. Journal of clinical pathology 47: 43–7; 1994. [PubMed: 7907609]

Drake RR, Powers TW, Jones EE, Bruner E, Mehta AS, Angel PM. MALDI Mass Spectrometry Imaging of N-Linked Glycans in Cancer Tissues. Advances in cancer research 134: 85–116; 2017. [PubMed: 28110657]

Duncan AL, Robinson AJ, Walker JE. Cardiolipin binds selectively but transiently to conserved lysine residues in the rotor of metazoan ATP synthases. Proceedings of the National Academy of Sciences of the United States of America 113: 8687–92; 2016. [PubMed: 27382158]

Farese AM, Brown CR, Smith CP, Gibbs AM, Katz BP, Johnson CS, Prado KL, MacVittie TJ. The ability of filgrastim to mitigate mortality following LD50/60 total-body irradiation is administration time-dependent. Health Phys 106: 39–47; 2014. [PubMed: 24276548]

Farese AM, Cohen MV, Katz BP, Smith CP, Gibbs A, Cohen DM, MacVittie TJ. Filgrastim improves survival in lethally irradiated nonhuman primates. Radiat Res 179: 89–100; 2013. [PubMed: 23210705]

Farese AM, Cohen MV, Katz BP, Smith CP, Jackson W, 3rd, Cohen DM, MacVittie TJ. A nonhuman primate model of the hematopoietic acute radiation syndrome plus medical management. Health Phys 103: 367–82; 2012. [PubMed: 22929469]

Farese AM, Hankey KG, Cohen MV, MacVittie TJ. Lymphoid and Myeloid Recovery in Rhesus Macaques Following Total Body X-Irradiation. Health physics 109: 414–26; 2015. [PubMed: 26425902]

Fliedner TM, Dörr HD, Meineke V. Multi-organ involvement as a pathogenetic principle of the radiation syndromes: a study involving 110 case histories documented in SEARCH and classified as the bases of haematopoietic indicators of effect. The British Journal of Radiology Supplement_27: 1–8; 2005.

Gandara RM, Mahida YR, Potten CS. Regional differences in stem and transit cell proliferation and apoptosis in the terminal ileum and colon of mice after 12 Gy. International journal of radiation oncology, biology, physics 82: e521–8; 2012.

Garate J, Fernandez R, Lage S, Bestard-Escalas J, Lopez DH, Reigada R, Khorrami S, Ginard D, Reyes J, Amengual I, Barcelo-Coblijn G, Fernandez JA. Imaging mass spectrometry increased resolution using 2-mercaptobenzothiazole and 2,5-diaminonaphtalene matrices: application to lipid distribution in human colon. Analytical and bioanalytical chemistry 407: 4697–708; 2015. [PubMed: 25903024]

Garofalo M, Bennett A, Farese AM, Ward A, Taylor-Howell C, Cui W, Gibbs A, Lasio G, Jackson WI, MacVittie TJ. The Delayed Pulmonary Syndrome Following Acute High-dose Irradiation: A Rhesus Macaque Model. Health Physics 106: 56–72; 2014. [PubMed: 24276550]

Hankey KG, Farese AM, Blaauw EC, Gibbs AM, Smith CP, Katz BP, Tong Y, Prado KL, MacVittie TJ. Pegfilgrastim Improves Survival of Lethally Irradiated Nonhuman Primates. Radiation research 183: 643–55; 2015. [PubMed: 26035709]

Harvey A, Cole LM, Day R, Bartlett M, Warwick J, Bojar R, Smith D, Cross N, Clench MR. MALDI-MSI for the analysis of a 3D tissue-engineered psoriatic skin model. Proteomics 16: 1718–25; 2016. [PubMed: 27226230]

Holzlechner M, Strasser K, Zareva E, Steinhäuser L, Birnleitner H, Beer A, Bergmann M, Oehler R, Marchetti-Deschmann M. In Situ Characterization of Tissue-Resident Immune Cells by MALDI Mass Spectrometry Imaging. Journal of Proteome Research 16: 65–76; 2017. [PubMed: 27755872]

Hulme HE, Meikle LM, Wessel H, Strittmatter N, Swales J, Thomson C, Nilsson A, Nibbs RJB, Milling S, Andren PE, Mackay CL, Dexter A, Bunch J, Goodwin RJA, Burchmore R, Wall DM. Mass spectrometry imaging identifies palmitoylcarnitine as an immunological mediator during Salmonella Typhimurium infection. Sci Rep 7: 2786; 2017. [PubMed: 28584281]

Jackson IL, Xu P, Hadley C, Katz BP, McGurk R, Down JD, Vujaskovic Z. A preclinical rodent model of radiation-induced lung injury for medical countermeasure screening in accordance with the FDA animal rule. Health Phys 103: 463–73; 2012. [PubMed: 22929472]

Jennemann R, Kaden S, Sandhoff R, Nordstrom V, Wang S, Volz M, Robine S, Amen N, Rothermel U, Wiegandt H, Grone HJ. Glycosphingolipids are essential for intestinal endocytic function. The Journal of biological chemistry 287: 32598–616; 2012. [PubMed: 22851168]

Jones JW, Bennett A, Carter CL, Tudor G, Hankey KG, Farese AM, Booth C, MacVittie TJ, Kane MA. Citrulline as a Biomarker in the Non-human Primate Total- and Partial-body Irradiation Models: Correlation of Circulating Citrulline to Acute and Prolonged Gastrointestinal Injury. Health physics 109: 440–51; 2015. [PubMed: 26425904]

Jones JW, Jackson IL, Vujaskovic Z, Kaytor MD, Kane MA. Targeted Metabolomics Identifies Pharmacodynamic Biomarkers for BIO 300 Mitigation of Radiation-Induced Lung Injury. Pharmaceutical research 34: 2698–2709; 2017. [PubMed: 28971289]

Jones JW, Scott AJ, Tudor G, Xu PT, Jackson IL, Vujaskovic Z, Booth C, MacVittie TJ, Ernst RK, Kane MA. Identification and quantitation of biomarkers for radiation-induced injury via mass spectrometry. Health Phys 106: 106–19; 2014a. [PubMed: 24276554]

Jones JW, Tudor G, Bennett A, Farese AM, Moroni M, Booth C, MacVittie TJ, Kane MA. Development and validation of a LC-MS/MS assay for quantitation of plasma citrulline for application to animal models of the acute radiation syndrome across multiple species. Analytical and bioanalytical chemistry 406: 4663–75; 2014b. [PubMed: 24842404]

Jurchen JC, Rubakhin SS, Sweedler JV. MALDI-MS Imaging of Features Smaller than the Size of the Laser Beam. Journal of the American Society for Mass Spectrometry 16: 1654–1659; 2005. [PubMed: 16095912]

Kagan VE, Bayir HA, Belikova NA, Kapralov O, Tyurina YY, Tyurin VA, Jiang J, Stoyanovsky DA, Wipf P, Kochanek PM, Greenberger JS, Pitt B, Shvedova AA, Borisenko G. Cytochrome c/cardiolipin relations in mitochondria: a kiss of death. Free radical biology & medicine 46: 1439–53; 2009. [PubMed: 19285551]

Kagan VE, Tyurina YY, Tyurin VA, Mohammadyani D, Angeli JP, Baranov SV, Klein-Seetharaman J, Friedlander RM, Mallampalli RK, Conrad M, Bayir H. Cardiolipin signaling mechanisms: collapse of asymmetry and oxidation. Antioxidants & redox signaling 22: 1667–80; 2015. [PubMed: 25566681]

Kandasamy P, Zarini S, Chan ED, Leslie CC, Murphy RC, Voelker DR. Pulmonary Surfactant Phosphatidylglycerol Inhibits Mycoplasma pneumoniae-stimulated Eicosanoid Production from Human and Mouse Macrophages. The Journal of biological chemistry 286: 7841–7853; 2011. [PubMed: 21205826]

Kasahara A, Scorrano L. Mitochondria: from cell death executioners to regulators of cell differentiation. Trends in cell biology 24: 761–70; 2014. [PubMed: 25189346]

Kuronuma K, Mitsuzawa H, Takeda K, Nishitani C, Chan ED, Kuroki Y, Nakamura M, Voelker DR. Anionic Pulmonary Surfactant Phospholipids Inhibit Inflammatory Responses from Alveolar Macrophages and U937 Cells by Binding the Lipopolysaccharide-interacting Proteins CD14 and MD-2. The Journal of biological chemistry 284: 25488–25500; 2009. [PubMed: 19584052]

Le Rhun E, Duhamel M, Wisztorski M, Gimeno JP, Zairi F, Escande F, Reyns N, Kobeissy F, Maurage CA, Salzet M, Fournier I. Evaluation of non-supervised MALDI mass spectrometry imaging combined with microproteomics for glioma grade III classification. Biochimica et biophysica acta 1865: 875–890; 2017. [PubMed: 27890679]

Li XX, Tsoi B, Li YF, Kurihara H, He RR. Cardiolipin and its different properties in mitophagy and apoptosis. The journal of histochemistry and cytochemistry : official journal of the Histochemistry Society 63: 301–11; 2015. [PubMed: 25673287]

Lukowski JK, Weaver EM, Hummon AB. Analyzing Liposomal Drug Delivery Systems in Three-Dimensional Cell Culture Models Using MALDI Imaging Mass Spectrometry. Analytical chemistry 89: 8453–8458; 2017. [PubMed: 28731323]

MacVittie TJ, Bennett A, Booth C, Garofalo M, Tudor G, Ward A, Shea-Donohue T, Gelfond D, McFarland E, Jackson W, 3rd, Lu W, Farese AM. The prolonged gastrointestinal syndrome in rhesus macaques: the relationship between gastrointestinal, hematopoietic, and delayed multi-organ sequelae following acute, potentially lethal, partial-body irradiation. Health Phys 103: 427–53; 2012a. [PubMed: 22929471]

MacVittie TJ, Farese AM, Bennett A, Gelfond D, Shea-Donohue T, Tudor G, Booth C, McFarland E, Jackson W, 3rd. The acute gastrointestinal subsyndrome of the acute radiation syndrome: a rhesus macaque model. Health Phys 103: 411–26; 2012b. [PubMed: 22929470]

Mariadason JM, Nicholas C, L'Italien KE, Zhuang M, Smartt HJ, Heerdt BG, Yang W, Corner GA, Wilson AJ, Klampfer L, Arango D, Augenlicht LH. Gene expression profiling of intestinal epithelial cell maturation along the crypt-villus axis. Gastroenterology 128: 1081–8; 2005. [PubMed: 15825089]

Medhora M, Gao F, Glisch C, Narayanan J, Sharma A, Harmann LM, Lawlor MW, Snyder LA, Fish BL, Down JD, Moulder JE, Strande JL, Jacobs ER. Whole-thorax irradiation induces hypoxic respiratory failure, pleural effusions and cardiac remodeling. Journal of radiation research 56: 248–60; 2015. [PubMed: 25368342]

Michael Danielsen E, Hansen GH. Lipid raft organization and function in brush borders of epithelial cells (Review). Molecular membrane biology 23: 71–79; 2006. [PubMed: 16611582]

Nilsson A, Peric A, Strimfors M, Goodwin RJA, Hayes MA, Andren PE, Hilgendorf C. Mass Spectrometry Imaging proves differential absorption profiles of well-characterised permeability markers along the crypt-villus axis. Sci Rep 7: 6352; 2017. [PubMed: 28743866]

Numata M, Chu HW, Dakhama A, Voelker DR. Pulmonary surfactant phosphatidylglycerol inhibits respiratory syncytial virus–induced inflammation and infection. Proc Natl Acad Sci U S A 107: 320–325; 2010. [PubMed: 20080799]

Palmer AD, Griffiths R, Styles I, Claridge E, Calcagni A, Bunch J. Sucrose cryo-protection facilitates imaging of whole eye sections by MALDI mass spectrometry. Journal of Mass Spectrometry 47: 237–241; 2012. [PubMed: 22359334]

Paradies G, Paradies V, De Benedictis V, Ruggiero FM, Petrosillo G. Functional role of cardiolipin in mitochondrial bioenergetics. Biochimica et Biophysica Acta (BBA) - Bioenergetics 1837: 408–417; 2014. [PubMed: 24183692]

Peterson LW, Artis D. Intestinal epithelial cells: regulators of barrier function and immune homeostasis. Nature reviews Immunology 14: 141–53; 2014.

Petrosillo G, Colantuono G, Moro N, Ruggiero FM, Tiravanti E, Di Venosa N, Fiore T, Paradies G. Melatonin protects against heart ischemia-reperfusion injury by inhibiting mitochondrial permeability transition pore opening. American journal of physiology Heart and circulatory physiology 297: H1487–93; 2009. [PubMed: 19684190]

Planas-Iglesias J, Dwarakanath H, Mohammadyani D, Yanamala N, Kagan VE, Klein-Seetharaman J. Cardiolipin Interactions with Proteins. Biophysical journal 109: 1282–94; 2015. [PubMed: 26300339]

Plett PA, Sampson CH, Chua HL, Joshi M, Booth C, Gough A, Johnson CS, Katz BP, Farese AM, Parker J, MacVittie TJ, Orschell CM. Establishing a murine model of the hematopoietic syndrome of the acute radiation syndrome. Health Phys 103: 343–55; 2012. [PubMed: 22929467]

Potten CS, Al-Barwari SE, Searle J. Differential radiation response amongst proliferating epithelial cells. Cell and tissue kinetics 11: 149–60; 1978. [PubMed: 630578]

Potten CS, Booth C. The role of radiation-induced and spontaneous apoptosis in the homeostasis of the gastrointestinal epithelium: a brief review. Comparative biochemistry and physiology Part B, Biochemistry & molecular biology 118: 473–8; 1997.

Potten CS, Grant HK. The relationship between ionizing radiation-induced apoptosis and stem cells in the small and large intestine. British journal of cancer 78: 993–1003; 1998. [PubMed: 9792141]

Powers TW, Holst S, Wuhrer M, Mehta AS, Drake RR. Two-Dimensional N-Glycan Distribution Mapping of Hepatocellular Carcinoma Tissues by MALDI-Imaging Mass Spectrometry. Biomolecules 5: 2554–72; 2015. [PubMed: 26501333]

Raja V, Greenberg ML. The functions of cardiolipin in cellular metabolism-potential modifiers of the Barth syndrome phenotype. Chemistry and physics of lipids 179: 49–56; 2014. [PubMed: 24445246]

Roberts SA, Hendry JH, Potten CS. Intestinal crypt clonogens: a new interpretation of radiation survival curve shape and clonogenic cell number. Cell proliferation 36: 215–31; 2003. [PubMed: 12950390]

Samhan-Arias AK, Ji J, Demidova OM, Sparvero LJ, Feng W, Tyurin V, Tyurina YY, Epperly MW, Shvedova AA, Greenberger JS, Bayir H, Kagan VE, Amoscato AA. Oxidized phospholipids as biomarkers of tissue and cell damage with a focus on cardiolipin. Biochimica et biophysica acta 1818: 2413–2423; 2012a. [PubMed: 22464971]

Samhan-Arias AK, Ji J, Demidova OM, Sparvero LJ, Feng W, Tyurin V, Tyurina YY, Epperly MW, Shvedova AA, Greenberger JS, Bayir H, Kagan VE, Amoscato AA. Oxidized phospholipids as biomarkers of tissue and cell damage with a focus on cardiolipin. Biochimica et Biophysica Acta (BBA) - Biomembranes 1818: 2413–2423; 2012b. [PubMed: 22464971]

Santucci R, Sinibaldi F, Policelli F, Fiorucci L. Role of cardiolipin in mitochondrial diseases and apoptosis. Current medicinal chemistry 21: 2702–14; 2014. [PubMed: 24735357]

Sapandowski A, Stope M, Evert K, Evert M, Zimmermann U, Peter D, Page I, Burchardt M, Schild L. Cardiolipin composition correlates with prostate cancer cell proliferation. Molecular and cellular biochemistry 410: 175–85; 2015. [PubMed: 26314254]

Schild L, Lendeckel U, Gardemann A, Wiswedel I, Schmidt CA, Wolke C, Walther R, Grabarczyk P, Busemann C. Composition of molecular cardiolipin species correlates with proliferation of lymphocytes. Experimental biology and medicine (Maywood, NJ) 237: 372–9; 2012.

Schlame M, Ren M. Barth syndrome, a human disorder of cardiolipin metabolism. FEBS letters 580: 5450–5; 2006. [PubMed: 16973164]

Shea-Donohue T, Fasano A, Zhao A, Notari L, Yan S, Sun R, Bohl JA, Desai N, Tudor G, Morimoto M, Booth C, Bennett A, Farese AM, MacVittie TJ. Mechanisms Involved in the Development of the Chronic Gastrointestinal Syndrome in Nonhuman Primates after Total-Body Irradiation with Bone Marrow Shielding. Radiat Res 185: 591–603; 2016. [PubMed: 27223826]

Sillence DJ, Platt FM. Glycosphingolipids in endocytic membrane transport. Seminars in cell & developmental biology 15: 409–16; 2004. [PubMed: 15207831]

Steven RT, Bunch J. Repeat MALDI MS imaging of a single tissue section using multiple matrices and tissue washes. Analytical and bioanalytical chemistry 405: 4719–4728; 2013. [PubMed: 23515611]

Takemura N, Kawasaki T, Kunisawa J, Sato S, Lamichhane A, Kobiyama K, Aoshi T, Ito J, Mizuguchi K, Karuppuchamy T, Matsunaga K, Miyatake S, Mori N, Tsujimura T, Satoh T, Kumagai Y, Kawai T, Standley DM, Ishii KJ, Kiyono H, Akira S, Uematsu S. Blockade of TLR3 protects mice from lethal radiation-induced gastrointestinal syndrome. Nature Communications 5: 3492; 2014.

Tyurina YY, Tyurin VA, Kapralova VI, Wasserloos K, Mosher M, Epperly MW, Greenberger JS, Pitt BR, Kagan VE. Oxidative lipidomics of gamma-radiation-induced lung injury: mass spectrometric characterization of cardiolipin and phosphatidylserine peroxidation. Radiat Res 175: 610–21; 2011. [PubMed: 21338246]

Vergeade A, Bertram CC, Bikineyeva AT, Zackert WE, Zinkel SS, May JM, Dikalov SI, Roberts LJ, 2nd Boutaud O. Cardiolipin fatty acid remodeling regulates mitochondrial function by modifying the electron entry point in the respiratory chain. Mitochondrion 28: 88–95; 2016. [PubMed: 27085476]

Wang C, Faloon PW, Tan Z, Lv Y, Zhang P, Ge Y, Deng H, Xiong J-W. Mouse lysocardiolipin acyltransferase controls the development of hematopoietic and endothelial lineages during in vitro embryonic stem-cell differentiation. Blood 110: 3601–3609; 2007. [PubMed: 17675553]

Wang J, Shao L, Hendrickson HP, Liu L, Chang J, Luo Y, Seng J, Pouliot M, Authier S, Zhou D, Allaben W, Hauer-Jensen M. Total Body Irradiation in the "Hematopoietic" Dose Range Induces Substantial Intestinal Injury in Non-Human Primates. Radiat Res 184: 545–53; 2015. [PubMed: 26495870]

Wang TY, Liu M, Portincasa P, Wang DQH. New insights into the molecular mechanism of intestinal fatty acid absorption. European journal of clinical investigation 43: 1203–1223; 2013. [PubMed: 24102389]

Yang H, Wang X, Xiong X, Yin Y. Energy metabolism in intestinal epithelial cells during maturation along the crypt-villus axis. Sci Rep 6: 31917; 2016. [PubMed: 27558220]

Zhang J, Yu W, Ryu SW, Lin J, Buentello G, Tibshirani R, Suliburk J, Eberlin LS. Cardiolipins Are Biomarkers of Mitochondria-Rich Thyroid Oncocytic Tumors. Cancer Res 76: 6588–6597; 2016. [PubMed: 27659048]

Zhang P, Cui W, Hankey KG, Gibbs AM, Smith CP, Taylor-Howell C, Kearney SR, MacVittie TJ. Increased Expression of Connective Tissue Growth Factor (CTGF) in Multiple Organs After Exposure of Non-Human Primates (NHP) to Lethal Doses of Radiation. Health physics 109: 374–90; 2015. [PubMed: 26425899]
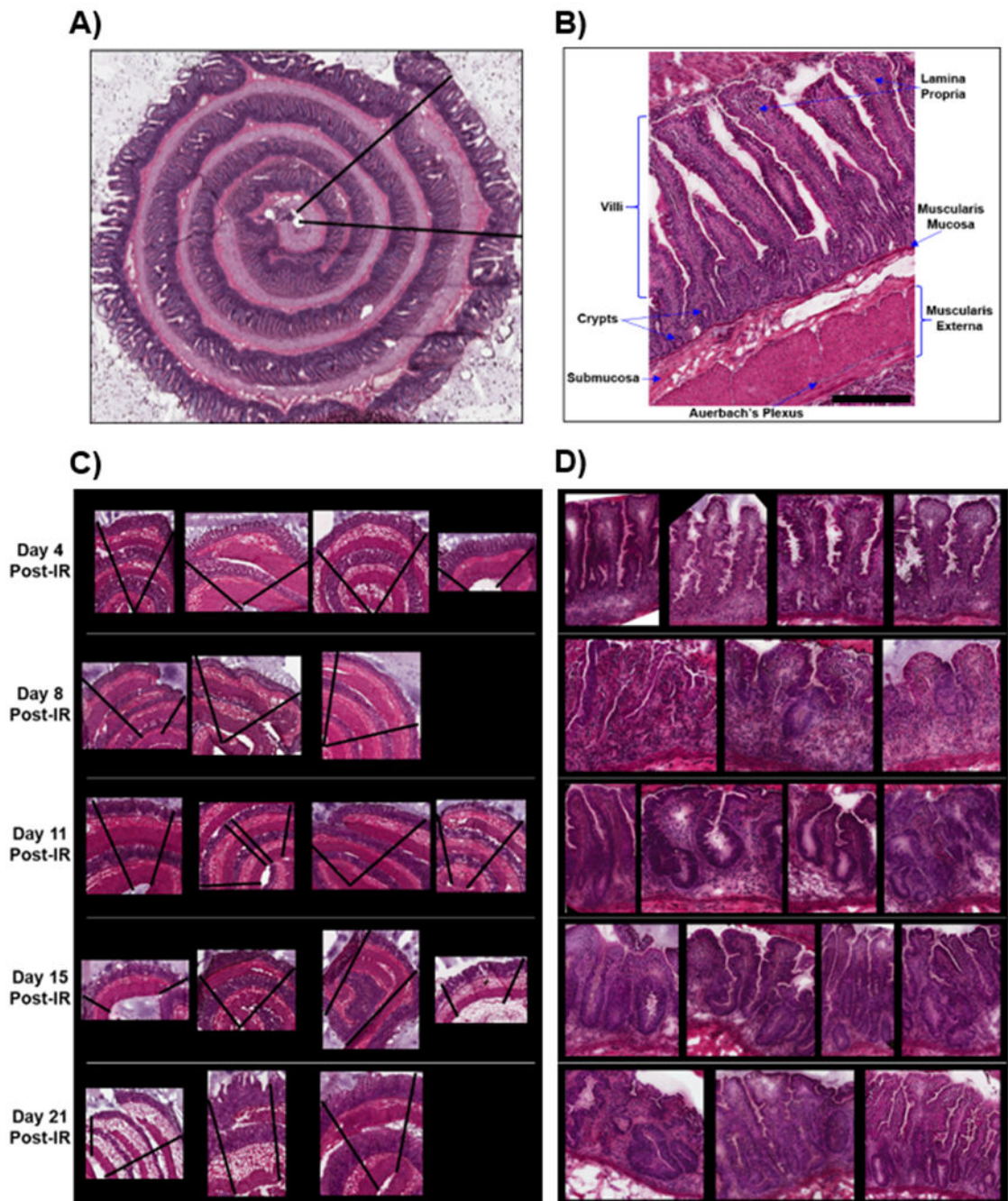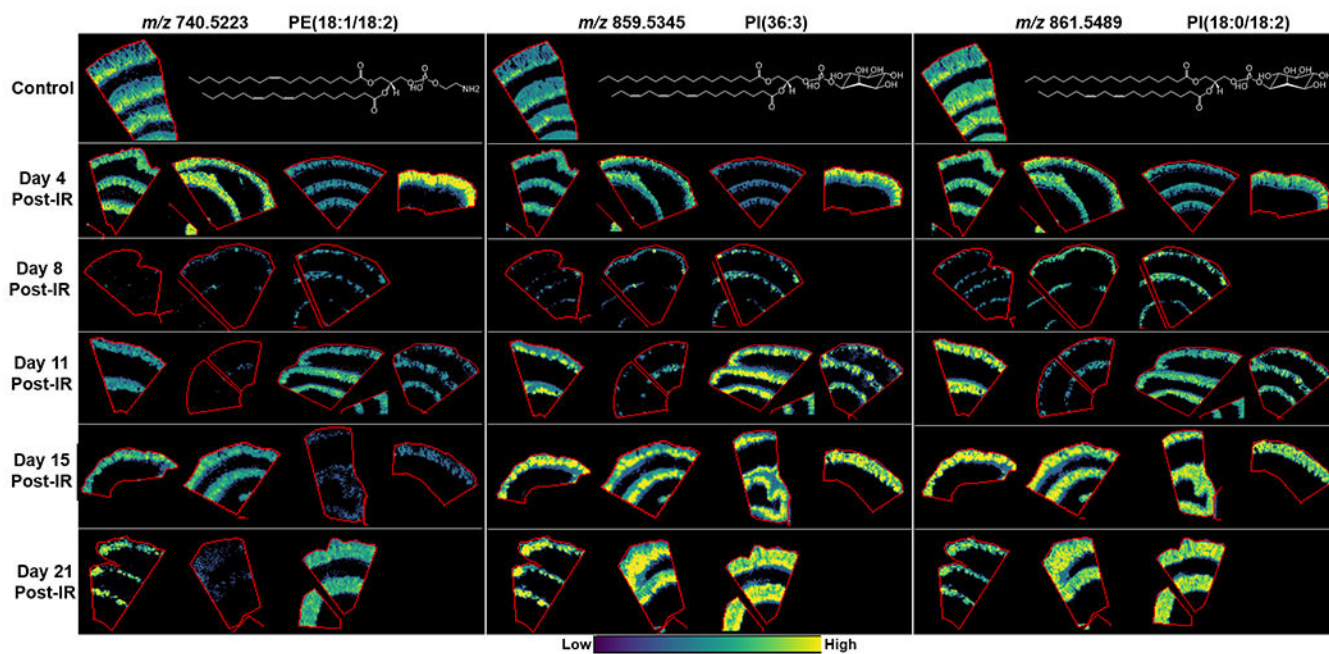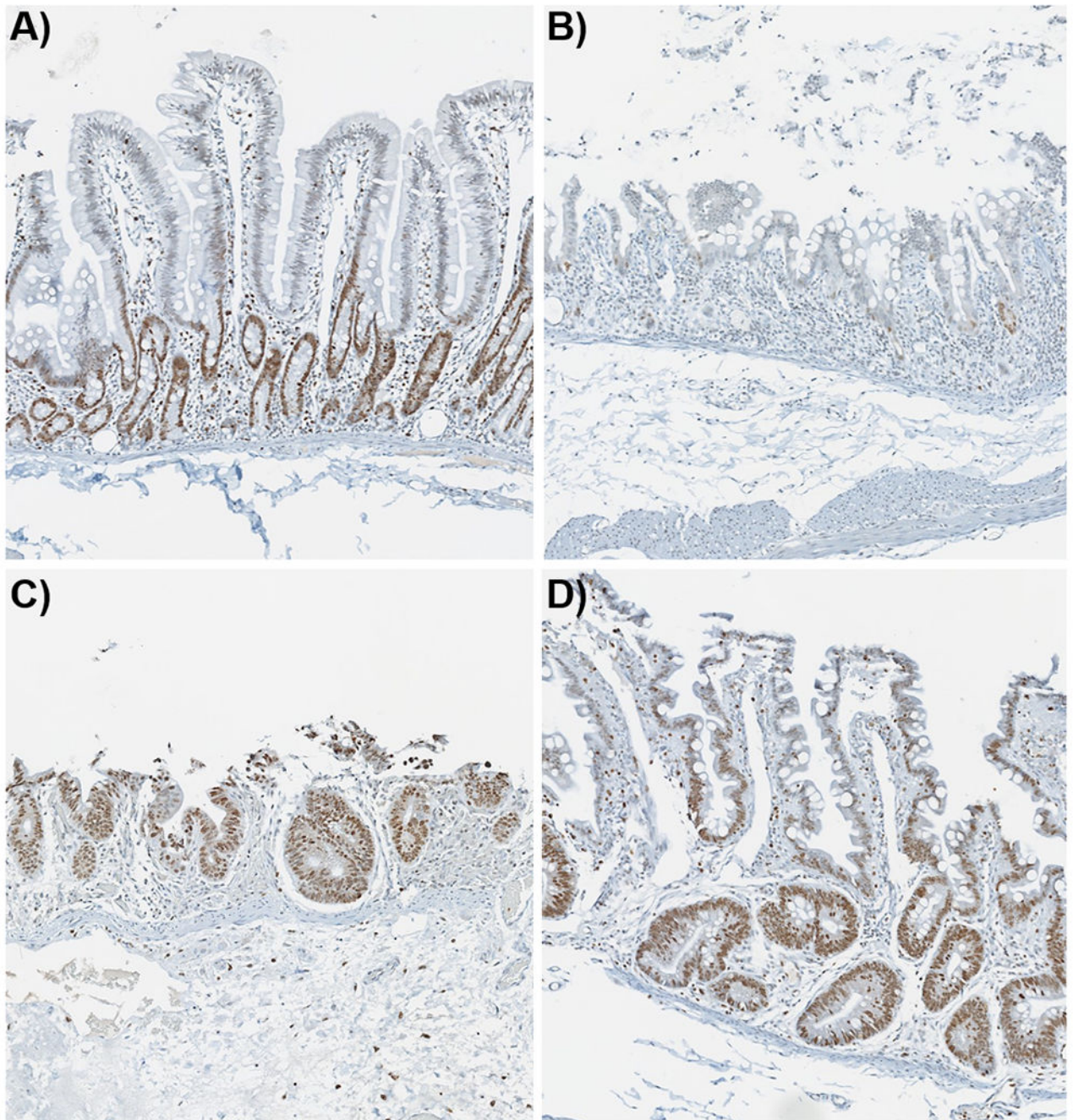
**Figure 1.**
Hematoxylin and eosin stained sections of the control jejunum in the Swiss roll orientation (A), a labeled higher magnification region of the control jejunum (B), irradiated jejunum rolls (C), and higher magnification of the irradiated jejunum samples (D). The black lines in figures A and C represent the regions scanned during MSI acquisition. Animal identification for each study day, from left to right; d4 (0191, 0809, 0827, 0261); d8 (0398, 0841, 0231) d11 (0869, 0432, 0871, 0829); d15 (0838, 0868, 0873, 0414) and d21 (9724, 0847, 0863).
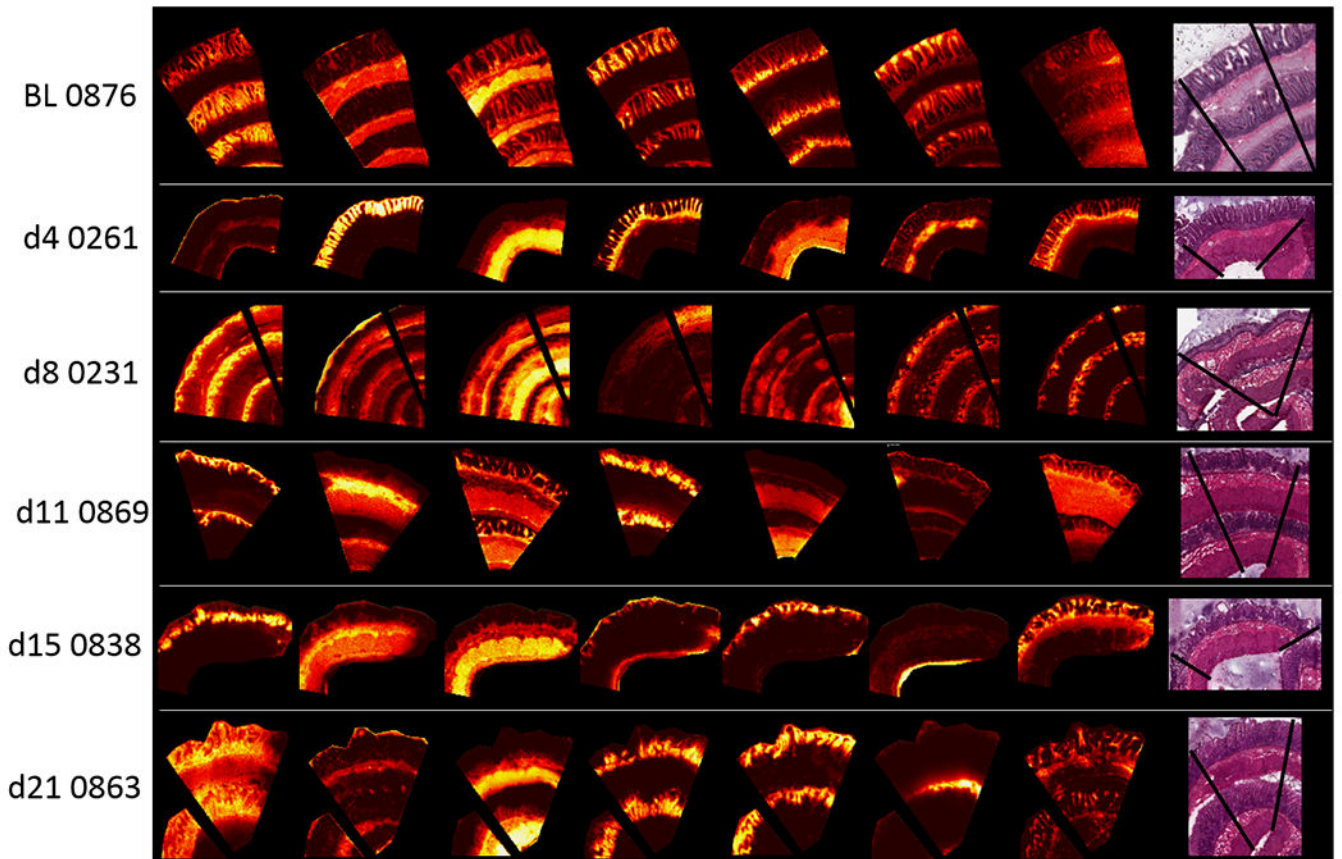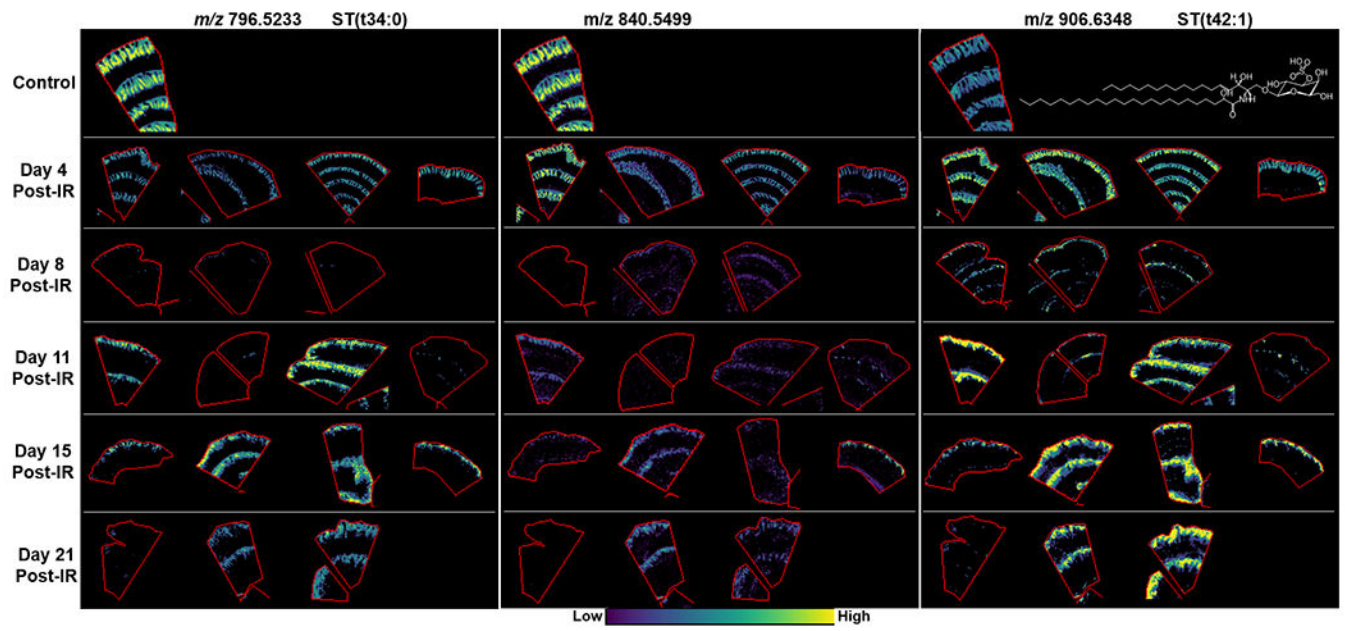
**Figure 2.**
Probabilistic latent semantic analysis (pLSA) score images showing 7 components from the control (BL 0876) and representative irradiated samples taken from each day post-IR. Their representative H&E stained sections are shown on the right.
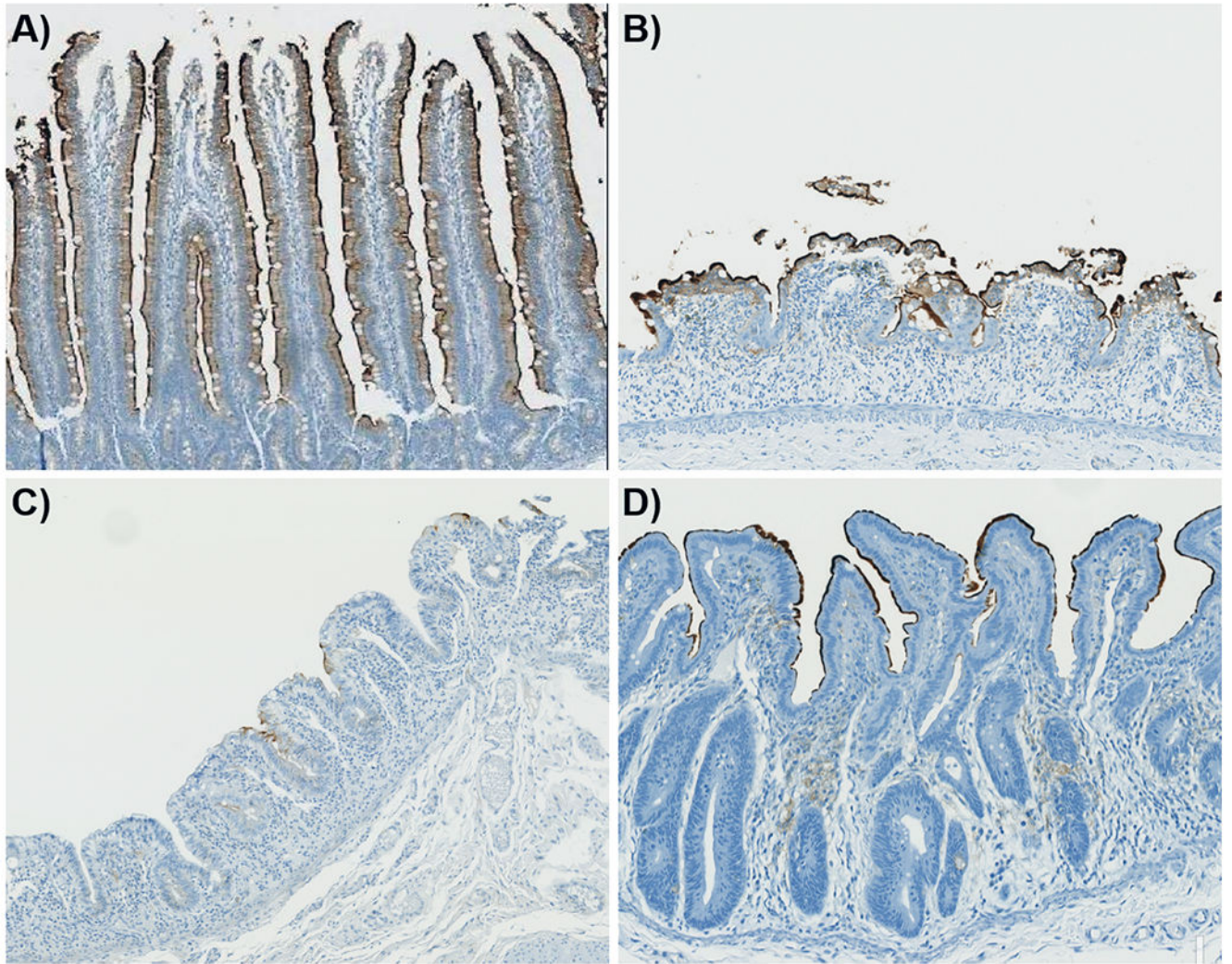
**Figure 3.**
MALDI-MS images of PE's and PI's localized to the crypt-villi axis in control and at days 4, 8, 11, 15 and 21 post-exposure. Example lipid structures are given, double bond positions are unknown, and PI(36:3) is a tentative structure based on the more commonly reported acyl chains for this species.

**Figure 4.**
Ki67 IHC stain with 3,3'-diaminobenzidine chromagen and hematoxylin counterstain. A) control animal displaying Ki67+ cells in the proliferating crypts, B) day 6 post-exposure showing very little staining along with the loss of crypts, C) day 9 post-exposure displays Ki67+ cells in the regenerating crypts and denuded villi, and D) Ki67+ staining in the hyperplastic crypts and the regenerated villi epithelium at day 29 post-exposure.

**Figure 5.**
MALDI-MS images of glycophosphingolipids mapped to the villi epithelium in control and days 4, 8, 11, 15 and 21 post-irradiation. Example lipid structures are given where possible.

**Figure 6.**
CD13 IHC labelling of the enterocyte apical surface (brush border) in the unirradiated
jejunal villi and at days 8, 11 and 19 post-exposure, for A-D, respectively.

**Figure 7.**
MALDI-MS images of PG's localized to the lamina Propria and muscularis externa in the control and at days 4, 8, 11, 15, and 21 post-exposure. Example lipid structures are given, double bond positions are unknown, and PG(34:0) is a tentative structure based on the more commonly reported acyl chains for this species.
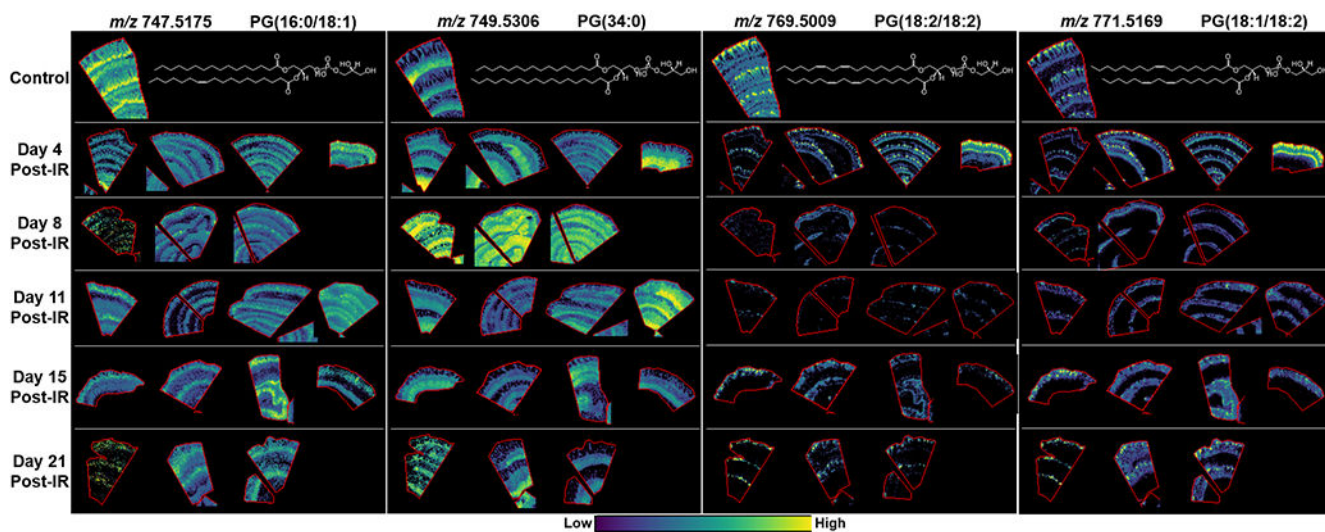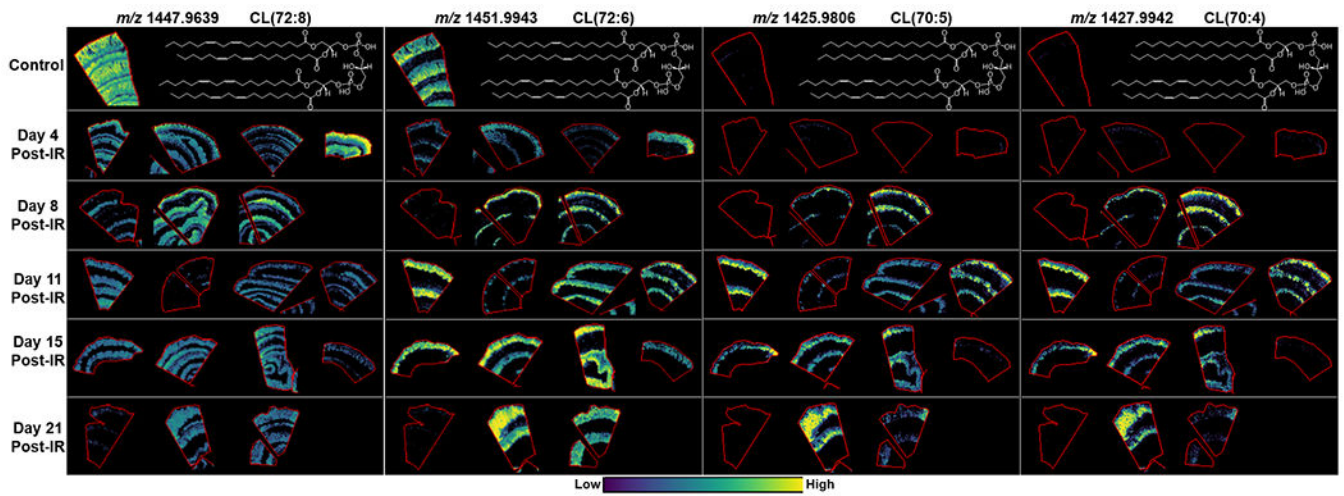
**Figure 8.**
MALDI-MS images of cardiolipins detected in the jejunum of control and irradiated animals taken at days 4, 8, 11, 15 and 21 post-exposure. Example lipid structures are given based on tentative assignments from database searches and the more commonly reported species.

**Table 1.**

Lipid detection and distribution along the crypt-villus axis. All ions listed are the [M-H]⁻.

| Measured m/z | Theoretical m/z | Error ppm | Tentative Identification | Normal Tissue Distribution |
|---|---|---|---|---|
| 714.5069 | 714.5079 | −1.43 | PE(16:0/18:2) | Crypt-villi axis, gradient increasing |
| 740.5223 | 740.5236 | −1.81 | PE(18:1/18:2) | Crypt-villi axis, gradient decreasing |
| 742.5383 | 742.5392 | −1.20 | PE(18:0/18:2) | crypt-villi axis |
| 744.5537 | 744.5549 | 0.0022 | PE(18:0/18:1) | Crypt-villi axis gradient, Muscularis externa |
| 796.5840 | 796.5862 | −2.74 | PE(40:3) | Crypt-villi axis, gradient decreasing |
| 809.5176 | 809.5186 | −1.28 | PI(32:0) | Villi epithleium, low abundance crypts |
| 833.5172 | 833.5186 | −1.70 | PI(34:2) | crypt-villi epithelium |
| 835.5330 | 835.5342 | −1.39 | PI(34:1) | Crypt-villi axis, gradient decreasing |
| 857.5170 | 857.5186 | −1.84 | PI(36:4) | Crypt-villi axis, gradient increasing |
| 859.5345 | 859.5342 | 0.36 | PI(36:3) | Crypt-villi axis, gradient decreasing |
| 861.5489 | 861.5499 | −1.13 | PI(36:2) | Crypt-villi axis, gradient decreasing |
| 863.5653 | 863.5655 | −0.28 | PI(36:1) | Crypt-villi axis, gradient decreasing |
| 881.5180 | 881.5186 | −0.69 | PI(38:6) | Crypt-villi axis, gradient decreasing |
| 889.5818 | 889.5812 | 0.67 | PI(38:2) | Crypt-villi axis, gradient decreasing |
| 909.5511 | 909.5499 | 1.33 | PI(40:6) | Crypt-villi axis, gradient increasing |

**Table 2.**

Glycosphingolipid detection and distribution along the villi epithelium. All ions listed are the [M-H]⁻.

| Measured m/z | Theoretical m/z | Error ppm | Tentative Identification | Normal Tissue Distribution |
|---|---|---|---|---|
| 778.51296 | 778.5145 | −1.98 | ST(d18:1/16:0) | Villi epithelium |
| 780.52863 | 780.5301 | −1.88 | ST(d34:0) | Villi epithelium |
| 794.50791 | 794.5094 | −1.88 | ST(d18:1/16:0(2OH)) | villi epithelium |
| 796.52338 | 796.525 | −2.03 | ST(t34:0) | gradient from villi base |
| 812.51852 | | | | gradient from villi base |
| 840.54999 | | | | gradient from villi base |
| 868.5812 | | | | villi epthelium |
| 878.60252 | 878.6033 | −0.89 | ST(t40:1) | villi epthelium |
| 880.61903 | 880.6189 | 0.15 | ST(t40:0) | villi epthelium |
| 888.56969 | | | | villi tip |
| 890.63837 | 890.6397 | −1.49 | ST(d18:1/24:0) | villi epithlieum |
| 896.61293 | | | | villi epithelium |
| 904.6193 | 904.6189 | 0.44 | ST(d18:1/24:1(2OH)) | villi epithlieum |
| 906.63484 | 906.6346 | 0.26 | ST(d18:1/24:0(2OH)) | villi epithelium |
| 910.62931 | | | | villi epithelium |
| 920.61441 | | | | villi epithelium |
| 922.62941 | | | | villi epithelium |
| 924.65155 | | | | villi epithlieum |

Lipid detection and distribution in the lamina propria (LP) and muscularis layers. All ions listed are the [M-H]⁻.

| Measured m/z | Theoretical m/z | Error ppm | Tentative Identification | Normal Tissue Distribution |
|---|---|---|---|---|
| 616.4701 | 616.4712 | −1.72 | CerP(d34:1) | Muscualris mucosa, externa, submucosa, LP |
| 642.4858 | 642.4868 | −1.59 | CerP(d36:2) | Muscualris mucosa, externa, submucosa, LP |
| 747.5175 | 747.5182 | −1.00 | PG(16:0/18:1) | Lamina propria - crypt region and lower villi, muscularis externa |
| 749.5306 | 749.5338 | −4.27 | PG(34:0) | Muscualris mucosa, externa, submucosa, LP |
| 750.5421 | 750.5443 | −2.97 | PE(P-18:0/20:4) | Muscularis externa, lamina propria (low) |
| 752.5955 | 752.5964 | −1.16 | *CerP(d44:3)*/GlcCer(d16:2/22:0) | Muscularis externa, submucosa, LP |
| 754.6106 | 754.612 | −1.80 | *CerP(d44:2)*/GalCer(d16:1/22:0) | Muscularis externa, submucosa, LP |
| 766.5380 | 766.5392 | −1.58 | PE(18:0/20:4) | Muscularis externa, lamina propria (low) |
| 769.5009 | 769.5025 | −2.14 | PG(18:2/18:2) | Tip of lamina propria |
| 771.5176 | 771.5182 | −0.79 | PG(18:1/18:2) | Tip of lamina propria |
| 788.5430 | 788.5447 | −2.11 | PS(18:0/18:1) | Muscualris mucosa, externa, submucosa, LP |
| 792.5534 | 792.5549 | −1.92 | PE(40:5) | Muscularis externa, lamina propria |
| 794.5693 | 794.5705 | −1.56 | PE(40:4) | Muscularis, low signal in LP |
| 820.5850 | 820.5862 | −1.50 | PE(42:5)/PE(O-42:6(OH))/PE(P-42:5(OH)) | Muscularis externa, lamina propria |
| 883.5336 | 883.5342 | 0.0006 | PI(38:5) | Muscularis externa, lamina propria |
| 885.5497 | 885.5499 | 0.0002 | PI(18/20:4) | Muscularis externa, lamina propria |
| 911.5662 | 911.5655 | 0.75 | PI(40:5) | Muscularis externa, lamina propria |
| 913.5811 | 913.5812 | 0.0001 | PI(40:4) | Muscularis externa, lamina propria |

**Table 4.**

Cardiolipin detection and distribution. All ions listed are the [M-H]⁻.

| Measured m/z | Theoretical m/z | Error ppm | Tentative Identification | Normal Tissue Distribution |
|---|---|---|---|---|
| 1421.95098 | 1421.9493 | 1.18 | CL(70:7) | very low intensity in the crypt |
| 1423.96349 | 1423.965 | −1.06 | CL(70:6) | very low intensity in the crypt |
| 1425.98062 | 1425.9806 | 0.01 | CL(70:5) | very low intensity in the crypt |
| 1427.99415 | 1427.9963 | −1.51 | CL(70:4) | very low intensity in the crypt |
| 1445.94994 | 1445.9493 | 0.44 | CL(72:9) | very low intensity in the crypt fading up the villi |
| 1447.96393 | 1447.965 | −0.74 | CL(72:8) | Muscularis externa and villi epithelium, low crypt and submucosa |
| 1449.98041 | 1449.9806 | −0.13 | CL(72:7) | Crypt-villi axis, lower intensity in muscularis externa |
| 1451.99425 | 1451.9963 | −1.41 | CL(72:6) | Crypt, decreasing up the villus |
| 1454.00786 | 1454.0119 | −2.78 | CL(72:5) | Crypt |

**Table 5.**

Glycosphingolipid detection in nerve tissue. All ions listed are the [M-H]⁻.

| Measured m/z | Theoretical m/z | Error ppm | Tentative Identification | Normal Tissue Distribution |
|---|---|---|---|---|
| 778.57355 | 778.5756 | 0.0021 | PE(O-40:5)/PE(P-40:4) | Auerbach's plexus, muscularis, LP faint |
| 806.54422 | 806.5458 | 0.0015 | ST(d36:1) | Auerbach's Plexus |
| 878.60252 | 878.6033 | 0.0008 | ST(t40:1) | Auerbach's Plexus, villi epthelium |
| 888.6232 | 888.6240 | 0.0008 | ST(d42:2) | |
| 890.63837 | 890.6397 | 0.0008 | ST(d36:1) | Auerbach's Plexus |
| 904.6193 | 904.6189 | 0.44 | ST(t42:2) | Auerbach's Plexus, villi epithlieum |
| 906.63484 | 906.6346 | 0.26 | ST(t42:1) | Auerbach's Plexus, villi epithlieum |